ISSN 0915-633X

NATIONAL INSTITUTE FOR FUSION SCIENCE

X-ray Spectral Analysis of Yohkoh BCS Data on Sep. 6 1992 Flares - Blue Shift Component and Ion Abundances -

T. Kato, T. Fujiwara and Y. Hanaoka

(Received - Dec. 22, 1995)

NIFS-396 Feb. 1996

RESEARCH REPORT
NIFS Series

NAGOYA, JAPAN

X-ray spectral analysis of Yohkoh BCS data on Sep. 6 1992 flares
- Blue shift component and ion abundances -

Takako KATO and Tomoko FUJIWARA* and Yoichiro HANAOKA**

National Institute for Fusion Science, Nagoya, 464-01,Japan

*Dep. of Education, Aichi University of Education, Kariya, 448, Japan

**Nobeyama Radio Observatory, National Astronomical Observatory, Nobeyama, Nagano 384-13, Japan

ABSTRACT

We have studied the time evolution of BCS spectra of He - like S XV, Ca XIX and Fe XXV ions observed by the Yohkoh satellite for solar flares on 6th September 1992 at 05:05 (M2.4 class) and 08:59(M3.3 class). Electron temperatures are derived through the fit of the synthetic spectra to the observed ones. Apparent ion temperatures are derived from the line width of S XV and Ca XIX spectra. The blue shifted component in the rising phase is separated from the main component of the Ca XIX spectra. The emission measures are derived from the spectra without assuming ionization equilibrium and solar abundances for the first time. The time variation of these parameters are compared with hard X-rays, soft X-rays and radio measurements. In the preheating phase, the moderate increase of thermal plasma with turbulence indicated from the line width is observed. The time evolution of the blue shift component coincides with that of the burst in hard X-rays and microwaves which are produced by non - thermal high energy electrons. The ion density ratios derived from the spectra show a time - dependent non equilibrium ionization. They are shifted from the equilibrium values indicating an ionizing plasma.

Key words:

solar flares, X-ray spectroscopy, ion abundance, solar abundance, He-like ions

1. Introduction

Bragg crystal spectrometer (BCS) experiments on board the Yohkoh satellite launched in August in 1991 have been providing X-ray spectra of He-like Ca XIX, S XV and Fe XXV ions (Lang et al, 1992, Doschek et al, 1992). The Yohkoh BCS is about an order of magnitude more sensitive than previous X-ray flare spectrometers and is able to measure the early stages of flare in detail. The X-ray spectra are observed in the initial phase before the rapid increase of the flux. During the rising phase large line broadening of Ca XIX spectra are detected. An increase of the electron temperature from 1.4 to 2 keV in the rising phase is obtained by Fe XXV spectra. This detection was difficult with previous spectrometers. These measurements during the rise phase give new information which contain the flare model.

In this paper we present a detailed spectral analysis of time dependent BCS data for the solar flares on Sep. 6, 1992 at 05:05 (M2.4 class) and 08:59 (M3.3 class). These two flares give the very similar result from BCS spectra and we present mainly the analysis of the 05:05 flare which was observed also with soft X-ray telescope (SXT) and the hard X-ray telescope (HXT) on board Yohkoh and the Nobeyama Radioheliograph.

In the initial phase before the rising phase, the thermal emission are detected. In the rising phase very broad spectral shape of Ca XIX resonance line is observed. We separated the blue shift component from the main component in the rising phase and derived the ion temperatures and the emission measures. These parameters are compared with hard X-rays, microwaves and soft X-rays.

2. Atomic Data and model

We have constructed a code to calculate the synthetic spectra of He-like ions including satellite lines. This model is based on the collisional radiative (CR) model

of He-like ions (Fujimoto and Kato, 1984) for the line intensities emitted from the singly excited states. This model includes the recombination contribution from the H-like ions as well as the excitation from He-like ions for an arbitrary H/He - like ion abundance ratio. The dielectronic satellite lines as well as the inner shell satellite lines are added to the spectra. We also have included the continuum emission (free - free emission, free- bound emission) (Mewe et al, 1985, 1986) in the spectra. For the spectral fit, we did not assume the ionization equilibrium for the ion ratios, and the best spectral fit is obtained with non-equilibrium abundance ratios.

The excitation, the inner shell excitation, ionization and recombination rate coefficients have been evaluated by Itikawa et al(1995) for Yohkoh BCS data. We have used these data in our program. For the excitation rate coefficients of He-like S ions, the data by Zhang and Sampson (1990) are used for $1\ ^1S \rightarrow 2\ ^1P_1$, $2\ ^3P_J$ and $2\ ^1S_0$ and Nakazaki (1993) for $1\ ^1S \rightarrow 2\ ^3S_1$ transitions. For the dielectronic satellite lines the wavelengths and intensities calculated by Safronova given in Kato et al(1995) are used in this paper. The wavelengths of the excitation lines and the satellite lines by Safronova with MZ method and by Cornille with AUTLSJ method were compared in Kato et al(1995). The intensities of the satellite lines are also compared in this report. The temperatures derived using these two different atomic data sets differ by about 10%. For the inner shell excitation rate coefficients, data by Bely-Dubau et al (1982) for Li-like Fe ions and Itikawa et al (1995) for Li-like Ca and S ions are used respectively. For the inner shell excitation cross sections of Be-, B- and C-like Fe ions, the data by Safronova given in Kato et al(1995) are used.

For spectra of Fe XXV, the dielectronic satellite lines for n = 3 have wavelengths near the resonance line and have intensities much lower than those of the n = 2 satellite lines (j, k) as shown in Fig. 1. The inner shell satellite lines of Li-like, Be-like and B-like ions are shown by dotted curves in Fig.1. On the contrary, for S XV the intensities of dielectronic satellite lines for n = 3 are almost the same

as those of n = 2 satellite lines as shown in Fig.2. We can understand this from the fact that the intensities of the dielectronic satellite lines are proportional to Q_d,

$$Q_d = g(u)A_r A_a/(\Sigma A_a + \Sigma A_r) \qquad (1)$$

where A_r and A_a are the radiative transition probability and autoionization rate from the upper state and g(u) is the statistical weight of the upper state. For n = 2 satellite lines $Q_d \propto A_r \propto Z^4$ because $A_a > A_r$, on the contrary for n = 3 satellite lines, Q_d ~ constant because $A_a < A_r$, where Z is the charge of the ion. Then for n = 2 Q_d is much larger than for n = 3 for high Z ions, but for low Z the difference is small. In the He-like sulphur spectra obtained from Yohkoh, the forbidden line(z) and the n = 2 satellite lines (j, k) can not be resolved as shown in Fig.2, where the contribution of the dielectronic satellite lines are shown by dashed lines. Therefore in the case of Fe XXV spectra we derive T_e from the ratio of w to k,j while for S XV we use the ratio of w to n = 3 satellite lines.

3. BCS spectral analysis

A Voigt line profile is used for the spectral fit. The Lorenzian parameters for Fe XXV, Ca XIX and S XV derived from the observed spectra during the decay phase are 0.0003, 0.00013 and 0.00027A which give the FWHM 0.00015, .000075 and 0.000135 A, respectively. These values are compared to those expected from the crystal rocking curve, .000206, .0003889 and .00137A respectively (Fludra, 1994). The small additional broadening due to the noise of the electronics are assumed to have a Gaussian shape. The FWHM values are 0.000526A, 0.000294A and 0.0001A, respectively (Fludra, 1994). For Fe XXV spectra this broadening is not neglected to derive the ion temperature from the spectral broadening.

From the fit of the synthetic spectra to the observed spectra we can obtain

several plasma parameters as described in the following sub sections. Since the wavelengths are set for the flare at the center of the Sun, the observed wavelengths depends on the position of the flares and are generally shifted from the absolute values.

i) Electron temperature (T_e)

We have derived the electron temperature mainly from the intensity ratio of the satellite lines and the resonance line. For Fe XXV spectra, spectral range is rather wide from the He-like resonance line (1.85A) to the B-like satellite lines (1.89A) as shown in Fig. 1. For the southern hemisphere flares, we can measure C-like satellite lines. The temperature is derived mainly from the resonance line (w) and the dielectronic satellite lines (j). For Ca XIX spectra, the resolution is much better than Fe spectra and the spectral range is short from resonance line (3.177A) to the intercombination line(3. 2A). The electron temperature is mainly decided by the intensity ratio of the resonance line and the n = 3 dielectronic satellite lines near the resonance line. For S XV spectra the resonance line w (5.04A), intercombination lines x and y and the forbidden lines z (5.10A) are observed as shown in Fig.2. The wavelength of the n = 2 satellite lines are close to the forbidden lines and cannot be separated. Then the electron temperature is mainly decided by the n = 3 satellite lines as in the case of Ca XIX spectra. The intensity of the intercombination and forbidden lines are also temperature dependent and we use these intensity ratios for S XV spectra. We include H-like ions for the S XV spectral fit. The contribution of the recombination from H-like ions to the forbidden line is about 20% which is shown by dotted line in Fig.2.

ii) Ion temperature (T_i) and blue shifted component

The ion temperature is derived mainly from the broadening of the resonance line.

In the rising phase, Ca XIX spectra show much larger broadening than

expected from the electron temperature and the average wavelength of the resonance line is shifted to blue side comparing to that in the decay phase. We tried to fit the broadening with two components: a main component and a blue shifted component. The wavelength of the main component is fixed as that in the decay phase through all the time. The blue shifted component is determined to fit the rest of the main component. Then the wavelength shift, the apparent ion temperature and the intensity are obtained. We can derive the relative velocity of the blue shifted component from the shift of the wavelength to the main component.

The line widths of the S spectra change considerably from the beginning of the flare to the maximum as Ca spectra. It is considered that the lines from the different active regions overlap at the very early initial phase when the intensity of the lines from the flare are very low. There is an influence of turbulence on the line width in the rising phase.

iii) Ion abundance

a) I_W/I_C

From the intensity ratio of the resonance line (I_W) to the continuum (I_C), the ion abundance ratio n(He-like ion)/n(H) can be derived using the electron temperature obtained from the spectra, where n(He-like ion) and n(H) are the densities of He-like ion and hydrogen, respectively. In order to know the contribution of the spurious background in the continuum emission, we plotted the observed continuum intensity I_C of three spectra in the same period. The intensities of I_C(Fe XXV, ~1.83A) and I_C(Ca XIX, ~3.173A) are generally on the line of the same temperature in the rising phase and decay phase. I_C(S XV, ~5.08A) is generally larger than the intensity expected from I_C(Fe) and I_C(Ca). This is reasonable because I_C(S) is emitted from not only the solar flares but also from active regions where the temperature is low (500 eV), while I_C(Fe) and I_C(Ca)

come from only solar flares where the temperature is high (>1 keV). Then we can not use S spectra to derive the ratio n(He-like ion)/n(H).

b) I_w/I_s

From the intensity ratio of the resonance line (I_w) to the inner shell satellite lines (I_s ($1s^2\ 2s^n\ 2p^m$ -> $1s\ 2s^n\ 2p^{m+1}$)), the ion ratios can be derived. From Fe spectra we can derive the ion ratios of the n(Li-like), n(Be-like) and n(B-like) to n(He-like ion). From S spectra we can derive the ratio n(Li-like ion)/n(He-like ion) from the inner shell satellite line of Li-like ions.

For S spectral analysis we included the contribution of H-like ions through recombination, since the H-like ions are expected in high temperature plasma in solar flares. We did not assume ionization equilibrium to determine the ion abundances. All the ion density ratios are obtained from spectral fit.

iii) Volume emission measure (EM)

The observed line intensity I_w is written as,

$$I_w = \varepsilon_w n(\text{He-like ion}) n_e V/(4\pi r^2) \qquad \text{photons cm}^{-2}\ \text{s}^{-1}\ \text{sr}^{-1}$$

$$= \varepsilon_w (n(\text{He-like ion})/n(Z))(n(Z)/n(H))(n(H)/n_e) n_e^2 V/(4\pi r^2) \qquad (2)$$

$$= \varepsilon_w (n(\text{He-like ion})/n(H))(n(H)/n_e) n_e^2 V/(4\pi r^2) \qquad (3)$$

where ε_w is the emissivity ($\text{cm}^3\ \text{s}^{-1}$) of the line w, n_e electron density, n(Z) and n(H) are the densities of the element of Z and Hydrogen, V the volume where the line is emitted and r is the distance from the earth to the sun.

Usually the emission measure $n_e^2 V$ is derived assuming ionization

equilibrium for n(He-like ion)/n(Z) and element abundance for n(Z)/n(H) to be the solar abundance from eq.(2). But we have derived the emission measure from eq.(3) using the ion abundance n(He-like ion)/ n(H) derived from the spectra as described in the previous section without assuming the ionization equilibrium and solar abundance.

4. Time evolution of the plasma parameters

The time evolution of the integrated flux of the three different BCS spectra are shown in Fig.3(a) together with hard X-ray counting rate and microwave (17GHz) brightness in Fig.3(b) and (c). The fluxes of Fe XXV, hard X-ray and microwave show the similar time behaviour whereas those of Ca XIX and SXV delay. The dashed line in Fig. 3 (c) is the circular polarization degree measured in microwave (17GHz). Fig. 4 shows the images in soft X-rays, 17GHz microwaves and white light. Fig.4(a), (b) and (c) show the soft X-ray images for the initial phase, the rising phase and maximum phase, respectively. Fig.4 (d), (e) and (f) are comparison between the flare loop in soft X-rays (contour) and a 17GHz image in the initial phase, a white light image and a map of longitudinal B (magnetic field), respectively. We can see one of the foot point of the flare loop coincides with the sunspot where the magnetic field is strong. Furthermore this footpoint coincides with the radio source.

Time dependent spectra are classified into four phases as follows. We show the spectra of each phase in Fig. 5, 6 and 7 for Ca XIX, Fe XXV and S XV ions, respectively.

1) Initial phase (05:10 - 05:13)... Counting rates are very low, almost constant and increase gradually with time. The Ca XIX spectra show the line broadening of about 2 keV larger than the electron temperature which is around 1 keV. From the Fe XXV spectra from 05:12:00 - 14:00, T_e = 1.3 keV is obtained , although the statistics are bad. For S XV spectra, the higher ion temperature than Ca XIX are

observed but it is considered due to the contribution of other active regions. The emission measure in the initial phase is about 2 x 10^{47} cm^{-3} from Fe XXV and Ca XIX. The gradual increase of soft X-rays and microwaves are also observed during this period.

2) Rising phase (05:13 - 05:16)... Counting rate begins to increase very rapidly. The flux of Fe XXV increases very rapidly comparing to that of S XV. The flux of Fe XXV begins to decrease when the flux of Ca and S are still increasing as shown in Fig. 3 (a). This indicates that the high temperature plasma is made very rapidly and is cooled very rapidly as well. The electron temperatures increase following the increase of the counting rate. Line widths become broader than those in the initial phase and the blue shifted component appears obviously at the beginning of the rising phase. The hard X-rays which is considered to be produced by high energy electrons begins to increase rapidly almost at the same period. The hard X-ray counts reach the maximum value when the blue shifted component stops to increase. Time behavior of microwave brightness is similar to that of hard X-rays after the rising phase and the polarization degree of the radio source decreases down to 20 % until the maximum phase.

3) Maximum phase (05:16 - 05:18) ... Counting rates of Ca XIX and Fe XXV reach the maximum as well as the electron temperatures. Line widths of the main component become narrow indicating no turbulence. The blue shifted component is still seen but the ratio to the main component is small (about 20%). Hard X-ray and radio emission begin to decrease in the beginning of this phase.

4) Decay phase (05:18 - 05:25)... The electron temperature decreases from 2 keV to 1 keV as well as the counting rates. The ion temperature of Ca spectra becomes a little larger than that in the maximum phase to be around 1.6 keV.

i) Electron temperature (T_e)

The time evolution of the electron temperature

T_e derived from each ion are shown in Fig. 8. The maximum electron temperature from Fe XXV, T_e(Fe), is 2 keV at about 1 min. before the maximum of T_e(Ca). and 1 - 2 min. before the period when the counting rates are maximum. The value T_e(Fe) is higher than T_e(Ca) and T_e(Ca) is higher than T_e(S) in the rising phase. The value of T_e (S) in the initial phase is very low due to the contribution of other active regions but reaches the maximum to 1.6 keV in the maximum phase which is the temperature of the flare. The values of T_e(Fe) and T_e(Ca) coincide in the decay phase. The electron temperatures derived from the SXT data with A10.1μ and A112μ filters are also shown in Fig. 8. SXT total means the value from the whole flare region and SXT loop means only from the flare loop. The electron temperature derived from the SXT data is much lower than those from BCS data.

ii) Ion temperature (T_i)

Ca XIX spectra in the initial and rising phase show broad line width which indicate more than two blue shifted components (Doschek et al, 1992) as shown in Fig. 5. The average center of the wavelength of the resonance line in the rising phase is shifted to the blue side comparing to those in the decay phase. We tried to fit the spectra with two components; the main component and the blue shifted component. The wavelength of the main component is fixed as that in the decay phase through all the time. During the rising phase the apparent ion temperature of the main component is about 3 keV whereas that of the blue shifted one is around 6 keV which indicate the turbulence of 140 km/s and 220 km/s respectively. The relative velocity of the two components is derived to be 140 km/s from the wavelength shift of 1.4×10^{-3}A. The relative velocity goes down to 100 km/s towards the maximum phase.

The apparent ion temperatures derived from the main component of Ca XIX and S XV spectra are shown in Fig.9 together with the electron temperature as a

function of time. The ion temperature 2 keV from Ca XIX, T_i(Ca), in the initial phase indicates that the turbulence (100 km/s) begins before the increase of the X-ray flux. The line broadening including the main and the blue shifted component reaches the maximum value at the beginning of the rising phase (05:14) and decreases towards the maximum phase. The ion temperature decreases from 05:14 towards the maximum phase and reaches the value close to the electron temperature in the decay phase. This indicates the themalization occurs in the maximum phase. T_i(Ca) goes down and reaches the value to be around 1 keV lower than the electron temperatures T_e = 1.7 keV. This might be due to the saturation effect of the spectral shape due to the high counting rate. The larger value T_i(S) than T_i(Ca) in the initial and the rising phases is considered due to not only the effect of the turbulence but also the other active regions for S XV spectra.

iii) Emission measure (EM)

The volume emission measure n_e^2V is derived without assuming ionization equilibrium and solar abundance as explained in Sec. 3 (iii). The derived emission measures (EM) from two different spectra of Fe and Ca are shown in Fig. 10. The emission measure derived from S spectra, EM(S), has no meaning, since the continuum emission in S spectra includes the contribution of active regions and the intensity ratio I_w/I_c does not give th correct value n(Z)/n(H). The values of EM(Ca) and EM(Fe) agree well each other in all the phases including the rising phase. When the ionization equilibrium is assumed, the derived $[EM(Fe)]_{eq}$ from eq.(2) is generally smaller than $[EM(Ca)]_{eq}$ and $[EM(S)]_{eq}$ by more than factor of two. This indicates the non equilibrium ionization in solar flares as will be seen in the next section on abundances. In Fig. 10, the derived $[EM]_{eq}$ from only the line intensity assuming the ionization equilibrium are also plotted for Fe, Ca and S. The solar abundance for n(Fe)/n(H), n(Ca)/n(H) and n(S)/n(H) are taken to be 5 x

10^{-5}, 5 x 10^{-6} and 2 x 10^{-5}, respectively to derive $[EM]_{eq}$. The emission measures derived from SXT for the total flare and for the loop are also plotted in Fig.10. They are larger than those derived from BCS. This is considered due to the low temperature from SXT as shown in Fig.8.

It seems that the intensity of the blue shifted component reaches the maximum before the maximum phase and only the main component increases afterwards as shown in Fig.10. The ratio of the blue shifted component to the main component is about 20 - 30 % at the beginning and increases up more than 100%. But this ratio decreases from the end of the rising phase and the blue shifted component disappears in the main component after the maximum phase as shown in Fig.10. This behaviour is similar to hard X-ray and radio emission.

iv) Abundances

The density ratios n(Fe XXV)/n(H atom) and n(Ca XIX)/n(H atom) are derived from I_w/I_c as explained in Sec.3 (iv). They are plotted in Fig. 11 as a function of the electron temperature. The dotted lines in Fig. 11 indicate the ionization equilibrium values; $[n(\text{He-like})/n(H)]_{eq} = [n(\text{He-like})/n(Z)]_{eq}\ (n(Z)/n(H))$ where n(Z)/n(H) is solar abundance of the element Z. The values of abundance n(Z)/n(H) are written in the figures. The derived values in the rising phase and the decay phase are not the same for the same temperature. For S XV spectra, the continuum intensity includes the emission from lower temperature active regions than solar flare, although the line emission is emitted mainly from solar flare. Then the derived values of n(S XV)/n(H atom) do not give the correct values.

The ion density ratios n(Fe XXIV)/n(Fe XXV), n(Fe XXIII)/n(Fe XXV), n(Fe XXII)/n(Fe XXV), and n(S XIV)/n(S XV) are derived from the line intensity ratios of the inner shell satellite lines to the resonance line. The ratio of H-like ion to He-like ion, n(S XVI)/ n(S XV), is also derived from spectral fit mainly from the ratio of the resonance line and the forbidden line including the contribution of the

recombination from H-like S ions. The density of H-like ion is comparable to that of He-like ion after the maximum phase. The derived values are plotted as a function of electron temperatures for each ion in Fig. 12 (a) and (b). These values are derived only from the line intensity ratios without continuum emission. The ratios in ionization equilibrium are plotted by dotted lines. More detailed discussion will be in Sec. 6.

5. Comparison with Soft X-ray, Hard X-ray and Microwave data

i) Pre - heating

From Ca XIX and Fe XXV spectra, SXT data and radio emission, it is indicated that the thermal plasma around 1 keV is created in the initial phase (05:11 - 05:13) before the rapid increase of X-ray flux. This is so-called 'pre-heating'. Fig. 13 (a) shows the flux increase in the initial and rising phase. During the time period from 05:12:00 to 05:13:30 the soft X-ray flux shows a gradual increase and Fig. 4(b) shows that this increase corresponds to the slight brightening of the flare loop. The brightness at 17 GHz shows similar increase to the soft X-rays. By contrast, after 05:13:30, microwaves and hard X-rays show an abrupt increase due to non-thermal high energy electrons and soft X-ray brightening follows them.

Before the preheating (until 05:12) there has been a bright point at 17 GHz above the sunspot, which corresponds to one of the footpoint of the flare loop. The microwave emission from the sunspot is due to gyro-resonance emission from thermal plasma in a strong magnetic field; this emission shows strong polarization of about 50%. The strong polarization is kept during the pre-heating. This fact suggests that the radio emission during the pre-heating is also due to the thermal plasma, not due to the high energy electrons. The degree of polarization lowers to 20% after 05:14, since the microwaves in this period are mainly due to gyro-synchrotron emission by high energy electrons.

From the above results we conclude that the pre-heating is a thermal

phenomenon without high energy electrons. The analysis of Ca XIX spectra shows the higher ion temperature of 2 keV than the electron temperature 1 keV(Fig. 13(b)) because of the turbulence. Therefore the turbulent thermal plasma is created in the pre-heating phase.

ii) The rising phase and the blue shift component

In the rising phase the blue shifted component in Ca spectra begins to increase around at 05:13:30 and hard X-rays and microwaves begin to increase rapidly almost at the same period. The blue shifted component increases until the maximum phase. The hard X-ray counts reach the maximum value when the blue shifted component stops to increase at 05:16. The blue shift component shows a similar behaviour to the hard X-rays and the microwaves; this is consistent to the results of Bentley et al (1994). This fact suggests that the evaporation of chromospheric matter is correlated to the non - thermal electrons. The hard X-ray counts begins to decay earlier than BCS flux.

It is observed that hard X-ray and microwave fluxes begin to increase abruptly earlier than SXT by about 30 sec. as shown in Fig.13(a). Fe XXV flux increases rapidly similar to hard X-ray and S XV spectra increases slowly like the SXT data. This indicates that Fe XXV spectra are more correlated to high energy electrons than S XV spectra.

The time behaviour of the polarization degree is similar to that of the relative velocity of the blue shifted component obtained from Ca XIX which is shown in Fig. 13 (b). The decrease of the relative velocity of the blue shift component indicates the thermalization of the plasma.

6. Ion abundance and solar abundance

The density ratio n(Ca XIX)/n(H) and n(Fe XXV)/n(H) in the rising and the decay phases at the same temperature do not show the same value as shown in Fig.

11. The values in the rising phase is always smaller than those in the decay phase. Generally the value n(He-like)/n(H) increases in the rising phase and reach the maximum value near the temperature maximum. The period when the flux reaches the maximum is indicated as "peak" in the figures. Sylwester et al.(1984) interpreted this variation to be the abundance variation during the flare. We do not consider these variations due to the abundance variation but variation of the ionization degree. The dashed curves in Fig.11 show the ratios n(He-like)/n(H) in the ionization equilibrium assuming the solar abundances which are indicated in Figures. If we assume the solar abundance $n(Ca)/n(H) = 4 \times 10^{-6}$, and $n(Fe)/n(H) = 2 \times 10^{-5}$, the derived values are in the ionization equilibrium only for the period 05:16:17 - 05:17:47 and 05:15:47 - 05:17:47 for Ca and Fe ions, respectively. In the decay phase the ratios again deviate from the ionization equilibrium. This phenomena can not be interpreted in the closed system. Because the recombination time is less than 10 sec., the ion abundances should be always in ionization equilibrium in the decay phase. Therefore it is considered that there is some flow and/or escape of the highly ionized ions. Another possibility of the deviation is due to the high energy electrons. We will investigate these effects in the next paper.

If we assume the ionization equilibrium at the maximum phase when T_e reaches the maximum value, abundances are obtained to be $n(Ca)/n(H) = 4 \times 10^{-6}$ and $n(Fe)/n(H) = 2 \times 10^{-5}$ which are compared to the solar abundances $n(Ca)/n(H) = 3 \times 10^{-6}$ and $n(Fe)/n(H) = 4 \times 10^{-5}$ from Meyer (1985).

The ion abundance ratios n(Fe XXIV)/n(Fe XXV), n(Fe XXIII)/n(Fe XXV) and n(Fe XXII)/n(Fe XXV) derived from Fe XXV spectra are always larger than those in the ionization equilibrium as shown in Fig.12(a). This result indicates that the ionization balance is not in ionization equilibrium in solar flares although this problem has to be discussed more carefully with the atomic data (Itikawa et al, 1995, Kato et al 1995). We had the same results for the flare on January 21st. 1992

(Kato et al, 1993). Antonucci et al(1987) obtained the similar results from MSS BCS Fe spectral data. They interpreted the deviation due to the error of the ionization rate coefficients. We consider this is due to the non equilibrium ionization which are similar to the problem on the ratio n(He-like)/n(H). The plasma is considered to be in an ionizing phase even in the decay phase.

The emission measures derived from Ca and Fe spectra by eq.(3) without assuming the ionization equilibrium give the similar results as shown in Fig. 10. The emission measure $[EM(Fe)]_{eq}$ from Fe spectra by eq.(2) assuming the ionization equilibrium is smaller more than factor of three than that without assuming the ionization equilibrium as shown in Fig. 10 by a dashed line. This indicates also non equilibrium ionization for Fe ions.

7. Discussion

i) Energetics

The relation between the energy of non - thermal electrons and that of the thermal plasma is discussed here. Emission measures are derived without assuming the ionization equilibrium using the line intensity of the resonance line and the continuum. The values of EM(Fe) and EM(Ca) show almost the same values within 30% during all the phases. From EM = 10^{49} cm^{-3} at the maximum phase, using the scale of the flare 20000 km x 10000 km^2 (V = 2 x 10^{27} cm^3), the average electron density n_e = 7 x 10^{10} cm^{-3} is obtained. The thermal energy content, 3 $n_e k T_e V$ is 1 x 10^{30} erg for T_e = 1.7 keV. The thermal X-ray radiation energy of the flare is about 6 x 10^{28} erg for EM = 10^{49} cm^{-3} and the flare duration time = 10 min. The energy of the high energy electron (> 20 keV) estimated from hard X-ray flux is about 4 x 10^{28} erg/s at the peak point of the flux. This value gives

the electron energy about 3 x 10^{30} erg during the flare for 1 min. duration This shows that the non- thermal electron energy is comparable or larger than the thermal energy.

The total energy of high energy electron in the rising phase at 05:14:30 is 10^{28} erg/s. The energy of the blue shift component for the relative velocity of 100 km/s is estimated to be about 3 x 10^{27} erg at 05:14:30 using EM = 2 x 10^{48} cm^{-3} and V = 5 x 10^{26} cm^3 for the loop. The relative velocity can be increased if the direction of the blue shift component is not perpendicular to the surface. However we can say that the energy of the high energy electron is larger than that of the blue shift component. The thermal electrons in the rising phase is estimated to be 3 x 10^{37} electrons from the loop volume of SXT. The high energy electrons is expressed as 2 x $10^{41}E^{-5.8}$ electrons $(keV\ s)^{-1}$ from HXT. Using this spectrum the high energy electrons around 10 keV is about 4 x 10^{36} electrons for 10 seconds. This is about 10% of the thermal electrons in number.

ii) Ion abundances

The density ratios n(Ca XIX)/n(H) and n(Fe XXV)/n(H) show the time dependent history; the values in the rising phase are smaller than those in the decay phase..This indicates the non equilibrium ionization of He-like ions. The ion density ratios of Fe ions, n(Fe XXIV)/ n(Fe XXV), n(Fe XXIII)/n(Fe XXV) and n(Fe XXII)/ n(Fe XXV) are also shifted from the values in ionization equilibrium indicating ionizing plasmas. The derived value of n(Fe XXII)/ n(Fe XXV) is quite small comparing to other ion ratios as shown in Fig.12. This is due to the same wavelength of the dielectronic and inner shell satellite line of the B-like Fe ions We should investigate the wavelengths and rate coefficients more carefully for B-like Fe ions.

For the non equilibrium ionization problem, the effect of the differential emission measure has to be considered. In the rising phase

T_e(Fe), T_e(Ca) and T_e(S) are quite different and it is indicated the temperature distribution in the flare. However in the decay phase the derived T_e of three different ions show the almost same values. The deviation from the ionization equilibrium in the decay phase can not be explained by the differential emission measure. Therefore we consider the deviation is not due to the effect of the differential emission measure.

We are going to make a time dependent ionization model for a flare including the high energy electrons and/or the flow in solar flares.

Acknowledgement

The authors are grateful to Drs. K. Shibata, T. Fujimoto, J. Dubau and R. More for useful discussions. The authors would like to thank also Mr. M. Ohira and Ms. R. Igaue for spectral fit and graphs. The Mitaka Flare Telescope Group kindly provided us with the magnetograph data.

References

Antonucci, E., Dodero, M.A., Gabriel, A.H., Tanaka, K., Dubau, J., Astron. & Astrophys., 180, 263 (1987)

Bentley, R.D., Doschek, G.A., Simnett, G.M., Rilee, M.L., Mariske, J.T., Culhane, J.L., Kosugi, T. and Watanabe, T., Ap. J. , 421, L55 (1994)

Bely-Dubau, F., Dubau, J., Faucher P., Gabriel, A.H., M.N.R.A.S., 198 , 239(1982)

Doschek, G.A., Mariska, J.T., Watanabe, T. et al., PASJ, **44**, L95 (1992)

Fludra, A., private communication (1994)

Fujimoto, T. and Kato, T., IPPJ - 647 (1983), Phys. Rev. A 30, 379 (1984)

Itikawa, Y., Kato, T. and Sakimoto, K., The Institute of Space and Astronautical Science Report , No. 657, Japan (1995)

Kato, T., Safronova, U., Shlyaptseva, A., Cornille, M. and Dubau, J. , NIFS-DATA-24 (1995)

Kato, T., Masai, K., Sakimoto, K., Itikawa, Y., Watanabe, T., BCS group, Proceedings of the Fourth International Conference on Plasma Physics and Controlled Nuclear Fusion, esa sp-351,199 (1993)

Lang, J. et al, PASJ, 44, L55(1992)

Mewe et al, Astron. & Astrophys. Suppl, 62, 197 (1985)

Mewe, R., Lemen, J.R., van den Oord, G.H.J., Astron. & Astrophys. Suppl. Ser., vol.65, no.3, 511-36 (1986)

J- Paul. Meyer, Astrophys. J. Supp. 57, 172 (1985)

Nakazaki, S., Sakimoto, K., Itikawa, Y., Phys. Scripta, 47, 359 (1993)

Sterling, A.C., Doscheck, G.A. and Feldman, U., Ap. J. 404, 394 (1993)

Sylwester, J., Lemen, J.R. and Mewe, R. (1984) Nature, 310,665

Zhang, H.L. and Sampson, D.H. , Phys. Rev., A 42 , 5378 (1990)

Figure Captions

Fig.1 Fe XXV spectra in decay phase at 05:21:47 on September 6, 1992 flare. The dotted lines show the line intensities by the inner shell excitation of Li-like (q), Be-like (β) and B-like (I4) ions.

Fig.2 S XV spectra in decay phase at 05:23:02 on September 6, 1992 flare. The dashed line shows the intensities by the dielectronic satellite lines. The dotted line shows the contribution through the recombination from H-like ions.

Fig. 3 (a) Time evolutions of the integrated flux of Fe XXV, Ca XIX, and S X BCS spectra. The values of flux are normalized by the maximum flux value of each ion. (b) Time evolution of hard X-ray counts of the L, M1 and M2 bands of the HXT. (c) Time evolution of the brightness temperature and the degree of polarization at 17 GHz of the brightest point in the radio pictures.

Fig. 4 Images of the solar flare on September 6, 05:05 UT. Solar north is to the top, and each panel has a field of view of 2.6'x 2.6'. (a) - (c) Solar flare images taken by the SXT. An arrow in (b) shows the main flare loop. The three pictures are displayed in the same brightness scale except the region of the main flare loop in (c), which is extremely bright. (d) A radio picture at 17 GHz. (e) and (f) White light map and magnetogram of longitudinal B taken with the Flare Telescope at Mitaka. In the magnetogram the N and S polarities are displayed in white and black, respectively. The position of the main flare loop observed in soft X-rays is shown in (d) - (f) in contours.

Fig.5 Time evolution of BCS Ca XIX spectra. 1) Initial phase, 2) rising phase, 3) maximum phase and 4) decay phase. The dotted and dashed lines indicate the main and the blue shift component, respectively. Since the observed wavelengths depends on the position of the flare on the sun, they are generally shifted from the absolute values.

Fig.6 Time evolution of BCS Fe XXV spectra. 1) Initial phase, 2) rising phase, 3) maximum phase and 4) decay phase. The dotted curve indicate the

contribution of the inner shell excitation of Li, Be and B-like ions.

Fig.7 Time evolution of BCS S XV spectra. 1) Initial phase, 2) rising phase, 3) maximum phase and 4) decay phase.

Fig.8 Time evolution of the electron temperature derived from BCS Fe XXV, Ca XIX and S XV spectra. T_e derived from SXT are also shown.

Fig.9 Time evolution of the apparent ion temperature T_i from Ca XIX and S XV spectra. For Ca XIX the ion temperature of the main component is shown. The electron temperatures are also plotted as comparison.

Fig.10 The time evolution of the emission measures derived from Fe XXV, Ca XIX and SXV spectra. Solid and dotted lines with symbols are those obtained without assuming the ionization equilibrium using eq.(3), whereas the dashed and dot-dashed lines without symbols are those obtained using the ionization equilibrium with eq.(2).

Fig.11 The density ratio n(He-like ion)/n(H atom) as a function of the electron temperature. (a) n(Ca XIX)/ n(H) , (b) n (Fe XXV)/ n(H)

Fig.12 (a) Ion density ratios of Fe ions as a function of Te..
(b) Ion density ratios of S ions as a function of Te..

Fig. 13 Time evolutions in the initial and rising phases. (a) Fluxes in soft X-rays, hard X-rays, and microwaves. (b) Time evolutions of the degree of polarization at 17 GHz, the apparent ion temperature of the total linewidth including the blue shift and main components, and velocity of the blue shift component derived from Ca XIX spectra.

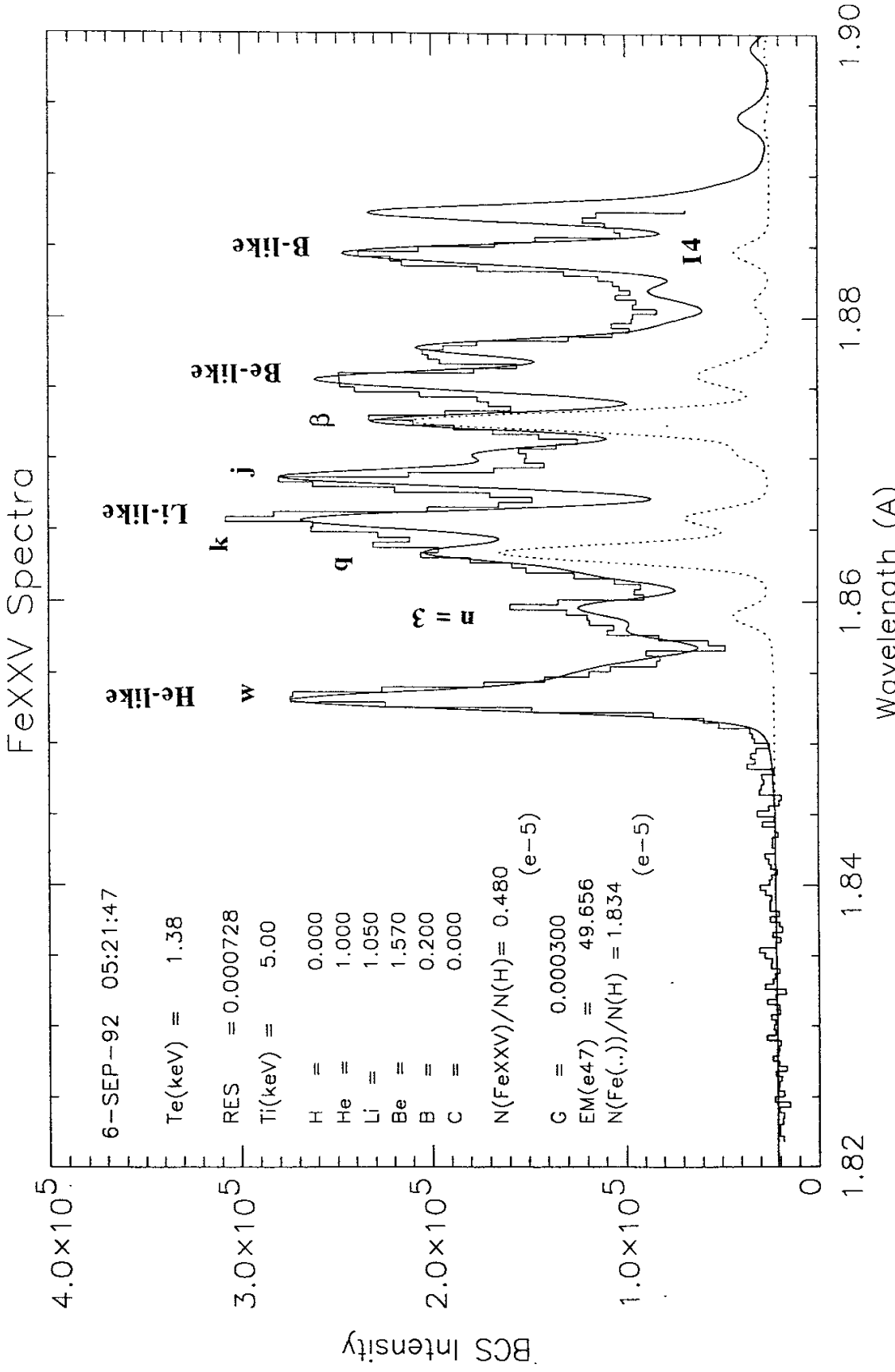
FeXXV Spectra
6-SEP-92 05:21:47
Te(keV) = 1.38
RES = 0.000728
Ti(keV) = 5.00
H = 0.000
He = 1.000
Li = 1.050
Be = 1.570
B = 0.200
C = 0.000
N(FeXXV)/N(H)= 0.480 (e-5)
G = 0.000300
EM(e47) = 49.656
N(Fe(..))/N(H) = 1.834 (e-5)
He-like
w
n = 3
q
k
Li-like
j
β
Be-like
B-like
I4
BCS Intensity
Wavelength (A)
4.0x10^5
3.0x10^5
2.0x10^5
1.0x10^5
0
1.82
1.84
1.86
1.88
1.90

Fig. 1

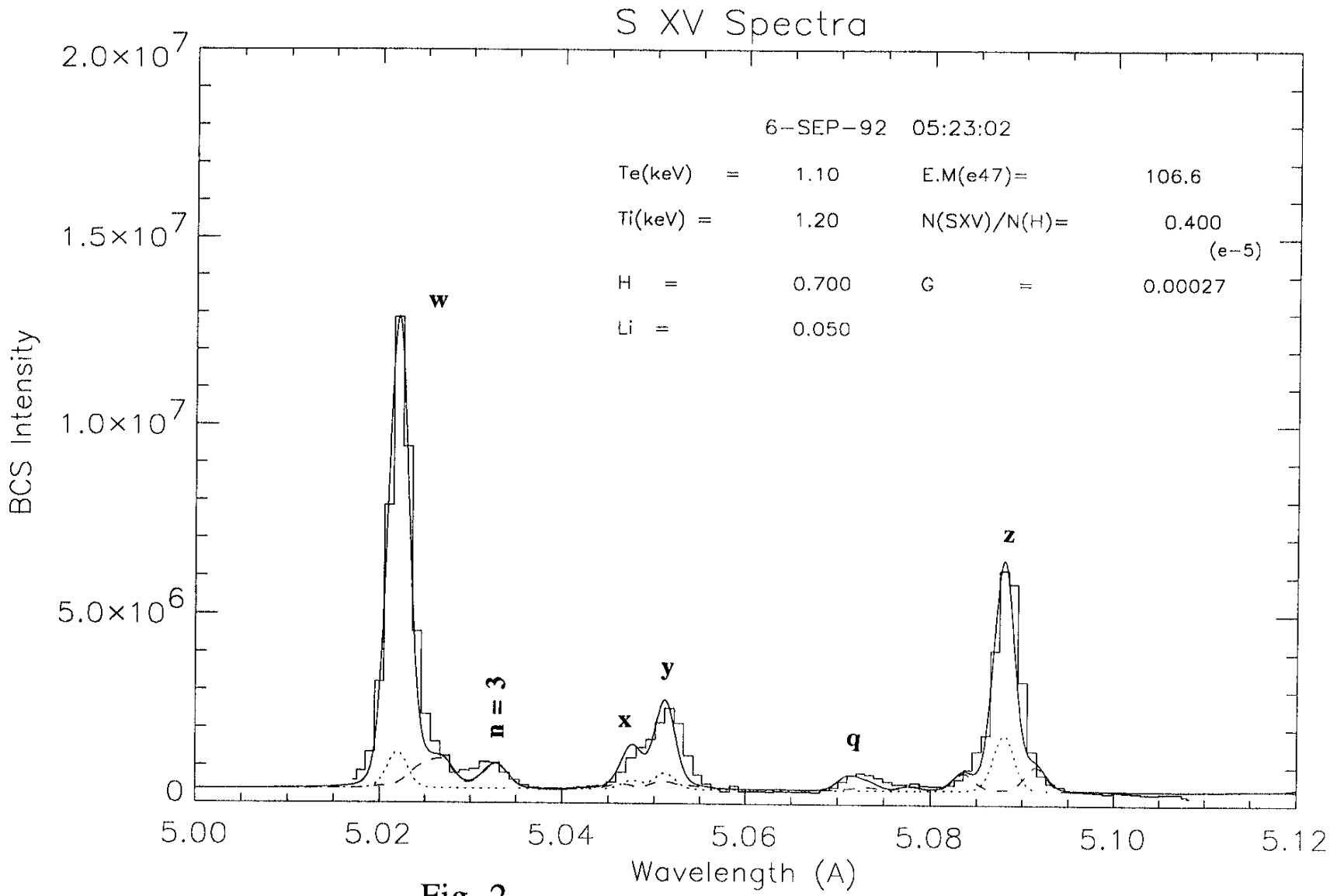
S XV Spectra
6-SEP-92 05:23:02
Te(keV) = 1.10
E.M(e47)= 106.6
Ti(keV) = 1.20
N(SXV)/N(H)= 0.400
(e-5)
H = 0.700
G = 0.00027
Li = 0.050
w
n = 3
x
y
q
z
BCS Intensity
2.0×10^7
1.5×10^7
1.0×10^7
5.0×10^6
0
5.00
5.02
5.04
5.06
5.08
5.10
5.12
Wavelength (A)

Fig. 2

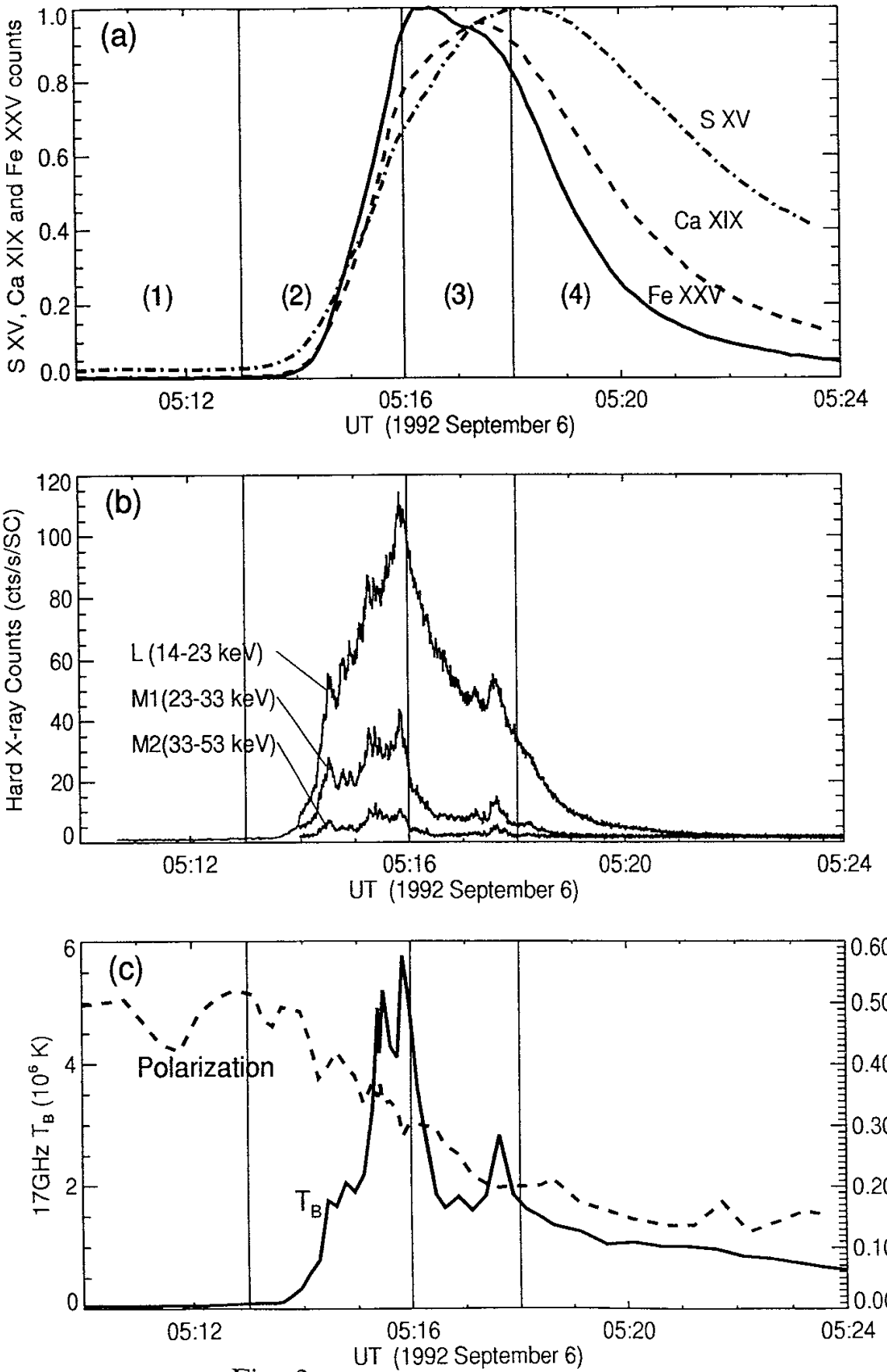
(a)
S XV, Ca XIX and Fe XXV counts
1.0
0.8
0.6
0.4
0.2
0.0
S XV
Ca XIX
Fe XXV
(1)
(2)
(3)
(4)
05:12
05:16
05:20
05:24
UT (1992 September 6)
(b)
Hard X-ray Counts (cts/s/SC)
120
100
80
60
40
20
0
L (14-23 keV)
M1(23-33 keV)
M2(33-53 keV)
05:12
05:16
05:20
05:24
UT (1992 September 6)
(c)
17GHz T_B (10^6 K)
6
4
2
0
Polarization
T_B
0.60
0.50
0.40
0.30
0.20
0.10
0.00
Polarization Degree
05:12
05:16
05:20
05:24
UT (1992 September 6)

Fig. 3

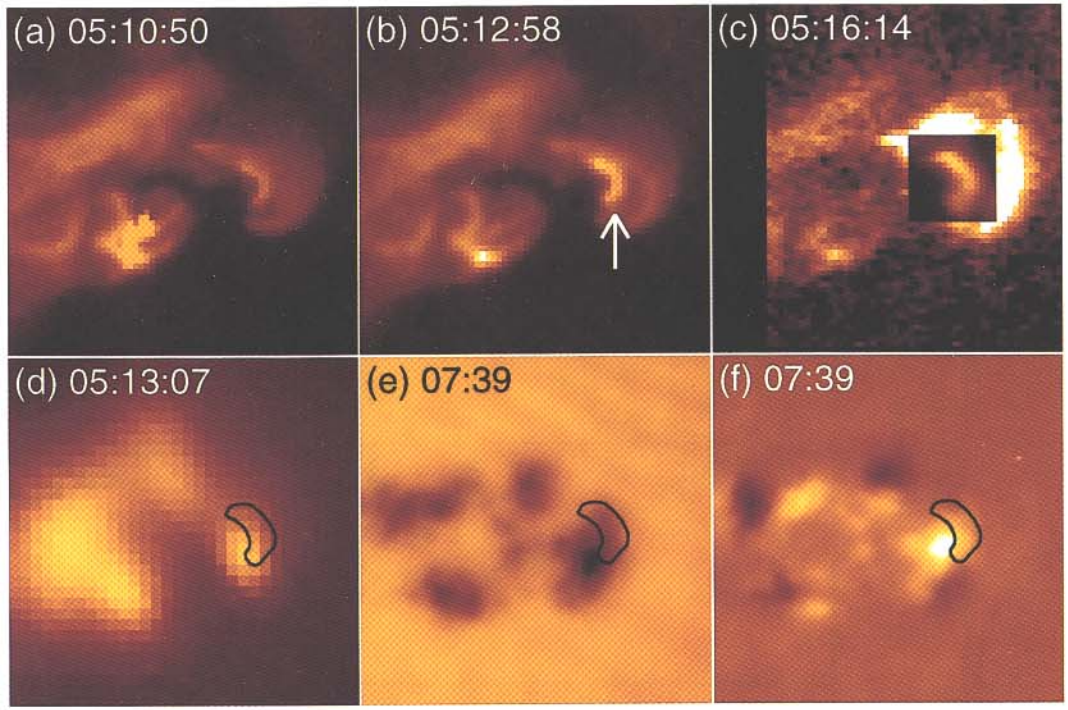

Fig. 4

Fig. 5

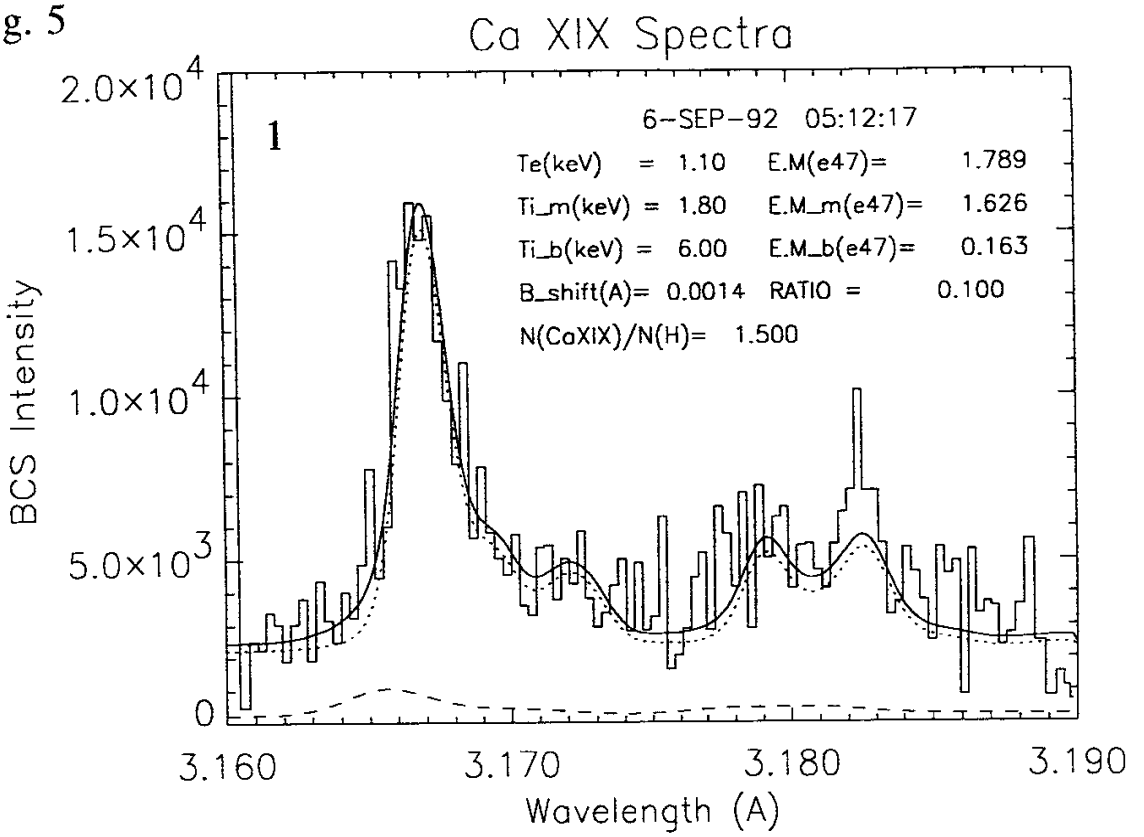
Ca XIX Spectra
1
6-SEP-92 05:12:17
Te(keV) = 1.10 E.M(e47)= 1.789
Ti_m(keV) = 1.80 E.M_m(e47)= 1.626
Ti_b(keV) = 6.00 E.M_b(e47)= 0.163
B_shift(A)= 0.0014 RATIO = 0.100
N(CaXIX)/N(H)= 1.500
BCS Intensity
2.0×10^4
1.5×10^4
1.0×10^4
5.0×10^3
0
3.160
3.170
3.180
3.190
Wavelength (A)

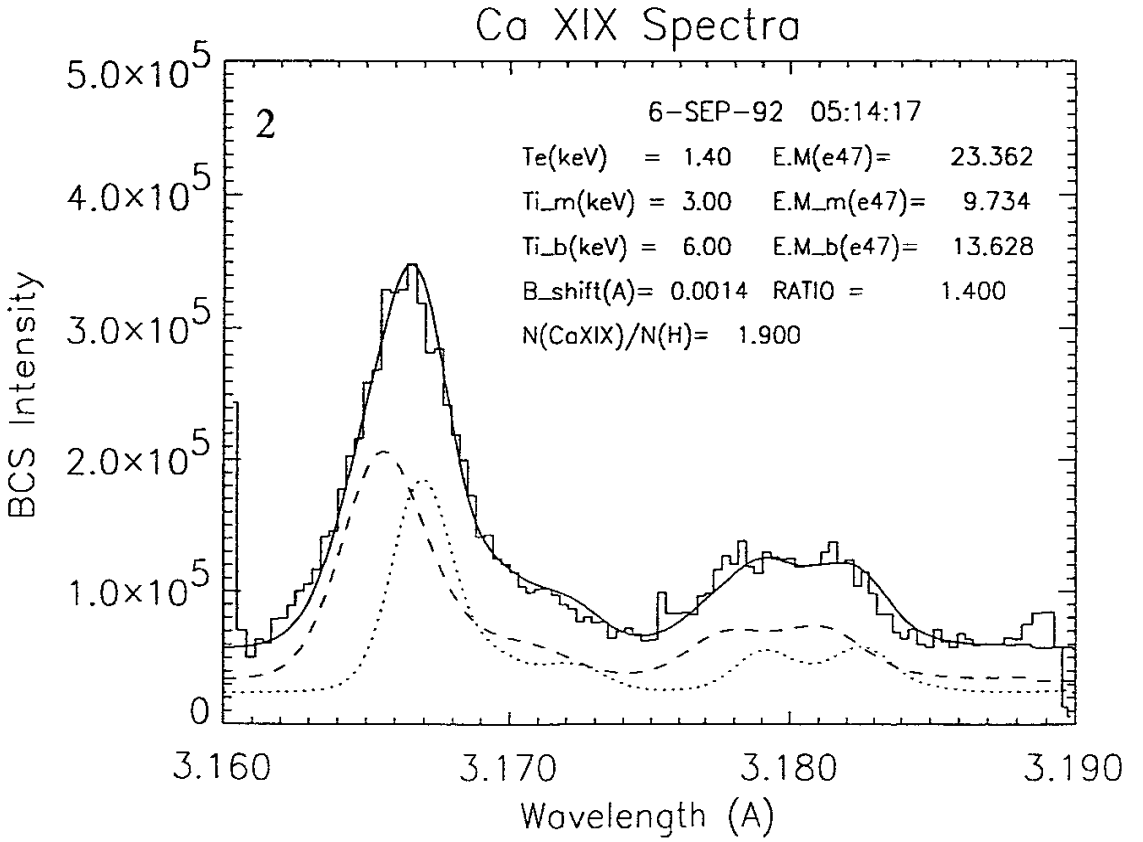
Ca XIX Spectra
2
6-SEP-92 05:14:17
Te(keV) = 1.40 E.M(e47)= 23.362
Ti_m(keV) = 3.00 E.M_m(e47)= 9.734
Ti_b(keV) = 6.00 E.M_b(e47)= 13.628
B_shift(A)= 0.0014 RATIO = 1.400
N(CaXIX)/N(H)= 1.900
BCS Intensity
5.0×10^5
4.0×10^5
3.0×10^5
2.0×10^5
1.0×10^5
0
3.160
3.170
3.180
3.190
Wavelength (A)

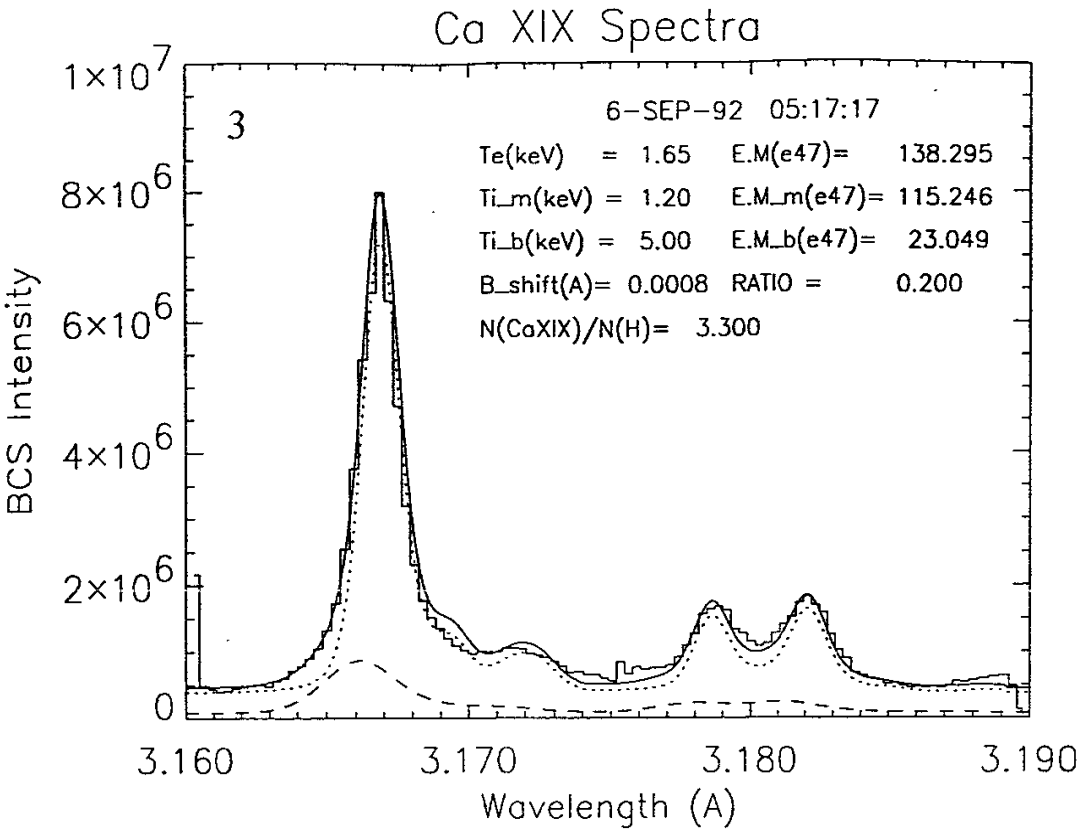
Ca XIX Spectra
3
6-SEP-92 05:17:17
Te(keV) = 1.65 E.M(e47)= 138.295
Ti_m(keV) = 1.20 E.M_m(e47)= 115.246
Ti_b(keV) = 5.00 E.M_b(e47)= 23.049
B_shift(A)= 0.0008 RATIO = 0.200
N(CaXIX)/N(H)= 3.300
BCS Intensity
1×10^7
8×10^6
6×10^6
4×10^6
2×10^6
0
3.160
3.170
3.180
3.190
Wavelength (A)

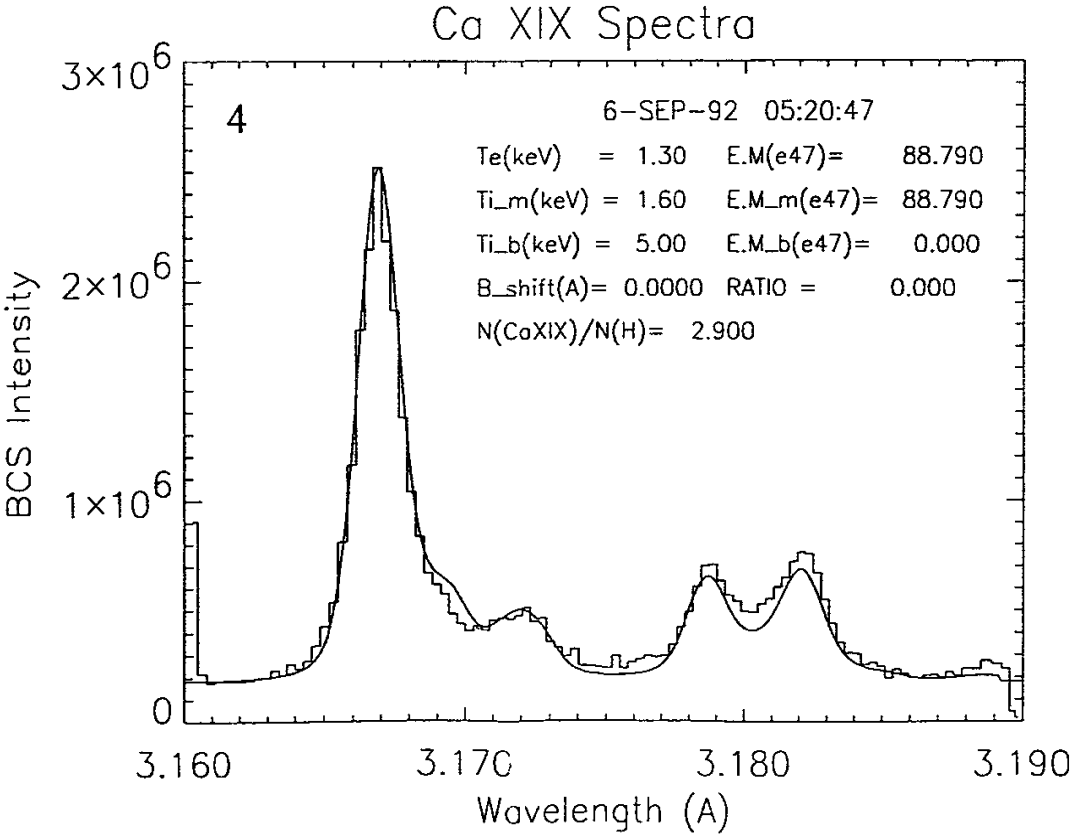
Ca XIX Spectra
4
6-SEP-92 05:20:47
Te(keV) = 1.30 E.M(e47)= 88.790
Ti_m(keV) = 1.60 E.M_m(e47)= 88.790
Ti_b(keV) = 5.00 E.M_b(e47)= 0.000
B_shift(A)= 0.0000 RATIO = 0.000
N(CaXIX)/N(H)= 2.900
BCS Intensity
3×10^6
2×10^6
1×10^6
0
3.160
3.170
3.180
3.190
Wavelength (A)

Fig. 6

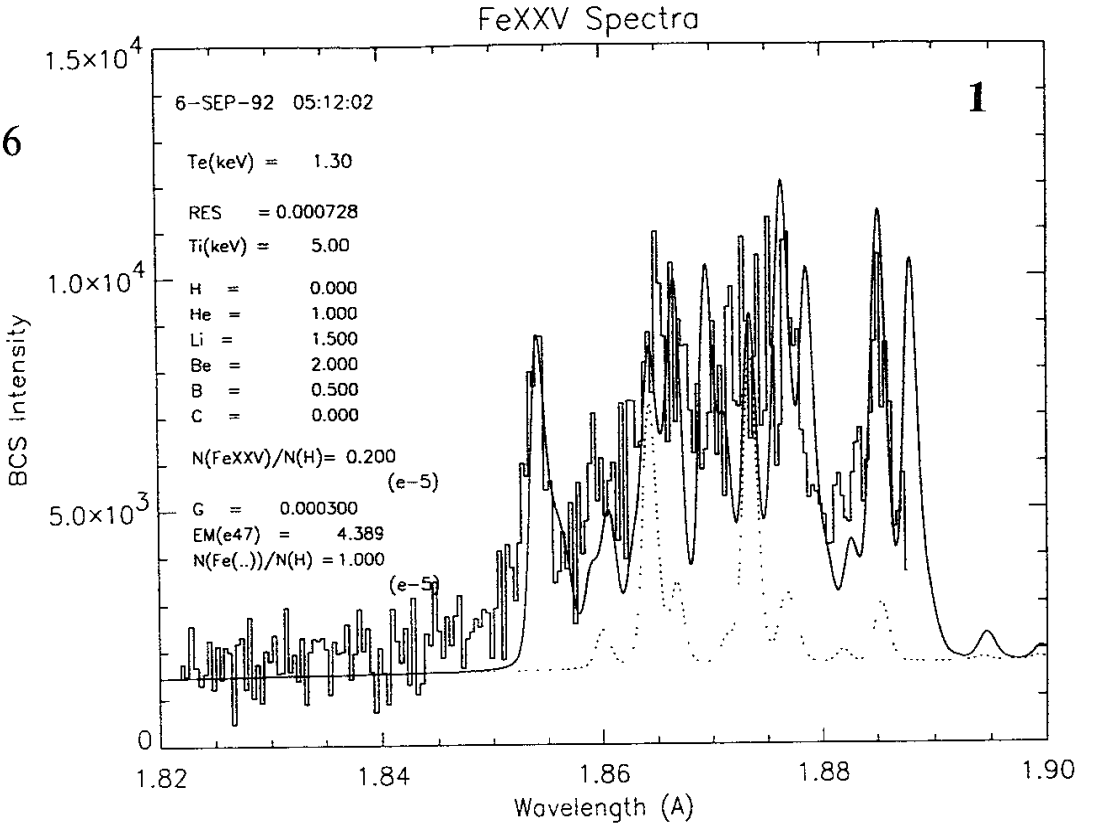
FeXXV Spectra
1
6-SEP-92 05:12:02
Te(keV) = 1.30
RES = 0.000728
Ti(keV) = 5.00
H = 0.000
He = 1.000
Li = 1.500
Be = 2.000
B = 0.500
C = 0.000
N(FeXXV)/N(H)= 0.200
(e-5)
G = 0.000300
EM(e47) = 4.389
N(Fe(..))/N(H) = 1.000
(e-5)
BCS Intensity
1.5×10^4
1.0×10^4
5.0×10^3
0
1.82
1.84
1.86
1.88
1.90
Wavelength (A)

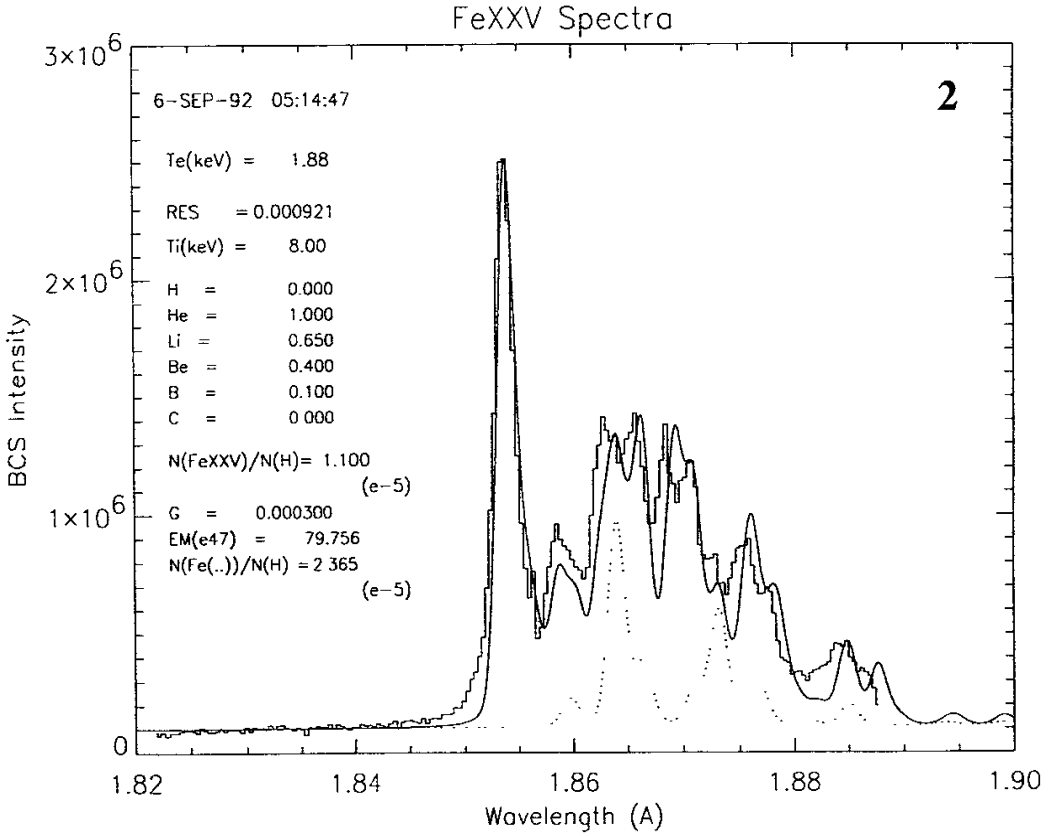
FeXXV Spectra
2
6-SEP-92 05:14:47
Te(keV) = 1.88
RES = 0.000921
Ti(keV) = 8.00
H = 0.000
He = 1.000
Li = 0.650
Be = 0.400
B = 0.100
C = 0.000
N(FeXXV)/N(H)= 1.100
(e-5)
G = 0.000300
EM(e47) = 79.756
N(Fe(..))/N(H) = 2.365
(e-5)
BCS Intensity
3×10^6
2×10^6
1×10^6
0
1.82
1.84
1.86
1.88
1.90
Wavelength (A)

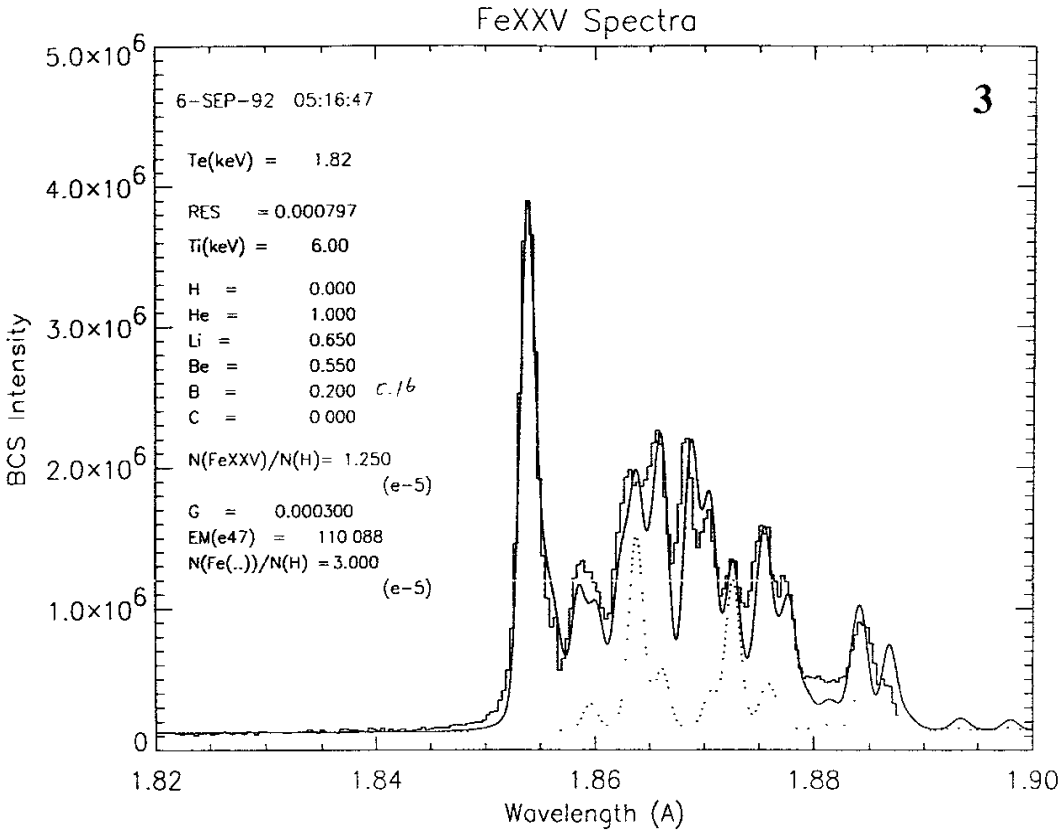
FeXXV Spectra
6-SEP-92 05:16:47
3
Te(keV) = 1.82
RES = 0.000797
Ti(keV) = 6.00
H = 0.000
He = 1.000
Li = 0.650
Be = 0.550
B = 0.200
C = 0.000
N(FeXXV)/N(H)= 1.250
(e-5)
G = 0.000300
EM(e47) = 110.088
N(Fe(..))/N(H) = 3.000
(e-5)
BCS Intensity
Wavelength (A)

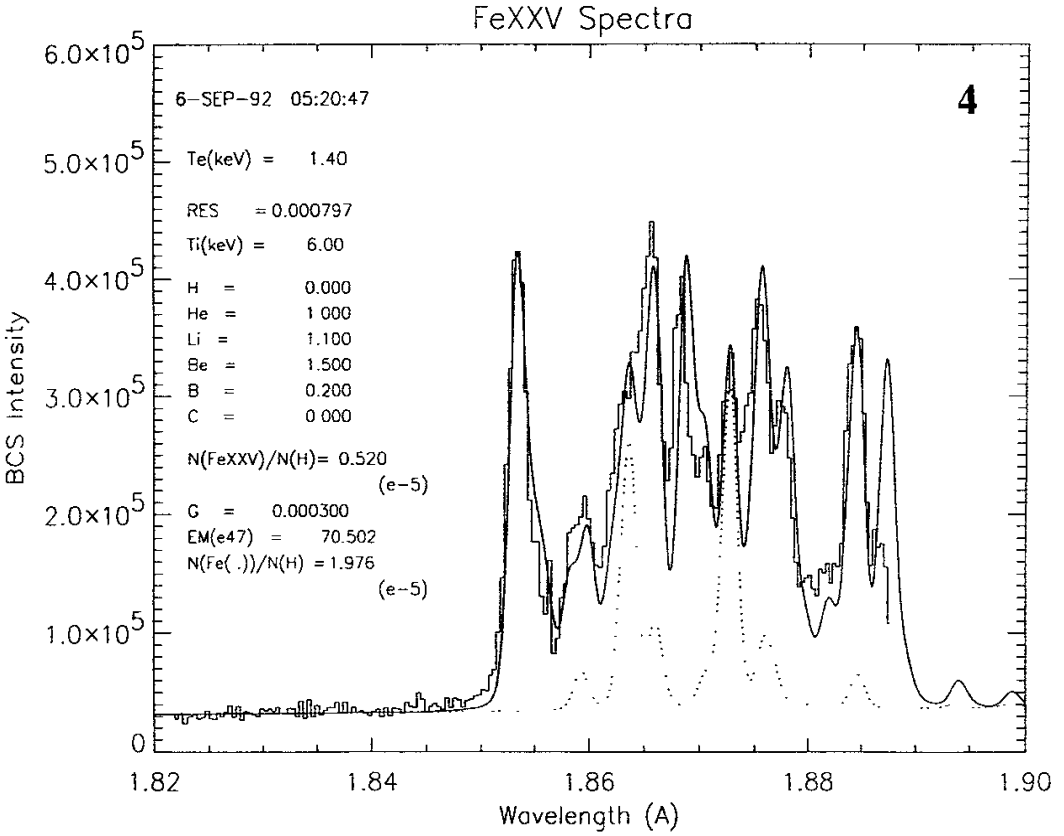
FeXXV Spectra
6-SEP-92 05:20:47
4
Te(keV) = 1.40
RES = 0.000797
Ti(keV) = 6.00
H = 0.000
He = 1.000
Li = 1.100
Be = 1.500
B = 0.200
C = 0.000
N(FeXXV)/N(H)= 0.520
(e-5)
G = 0.000300
EM(e47) = 70.502
N(Fe(..))/N(H) = 1.976
(e-5)
BCS Intensity
Wavelength (A)

Fig. 7

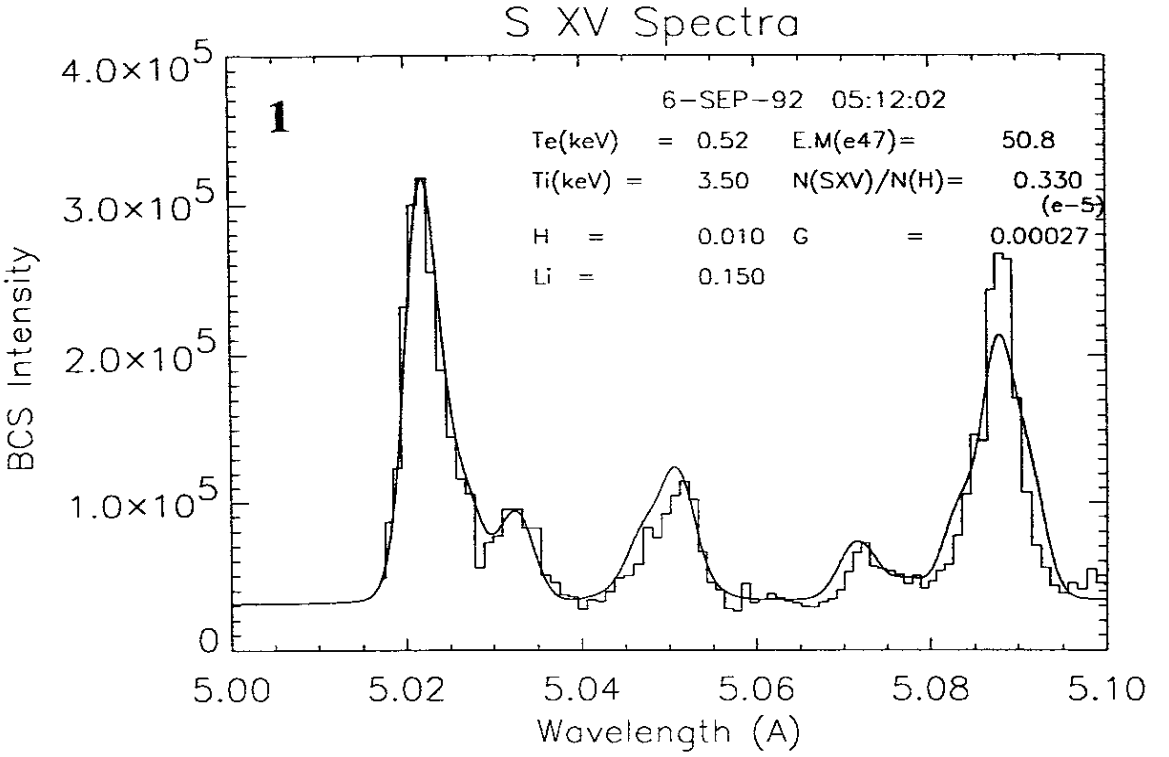
S XV Spectra
1
6-SEP-92 05:12:02
Te(keV) = 0.52 E.M(e47)= 50.8
Ti(keV) = 3.50 N(SXV)/N(H)= 0.330 (e-5)
H = 0.010 G = 0.00027
Li = 0.150
BCS Intensity
4.0×10^5
3.0×10^5
2.0×10^5
1.0×10^5
0
5.00
5.02
5.04
5.06
5.08
5.10
Wavelength (A)

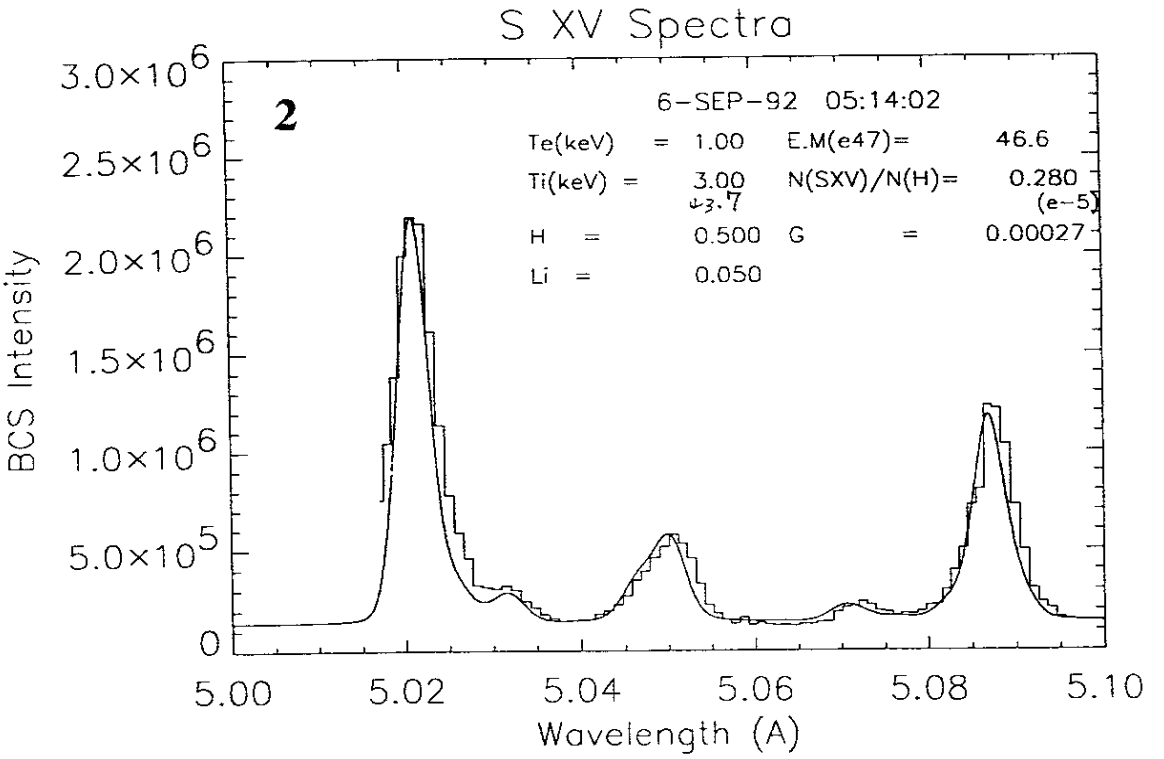
S XV Spectra
2
6-SEP-92 05:14:02
Te(keV) = 1.00 E.M(e47)= 46.6
Ti(keV) = 3.00 N(SXV)/N(H)= 0.280 (e-5)
H = 0.500 G = 0.00027
Li = 0.050
BCS Intensity
3.0×10^6
2.5×10^6
2.0×10^6
1.5×10^6
1.0×10^6
5.0×10^5
0
5.00
5.02
5.04
5.06
5.08
5.10
Wavelength (A)

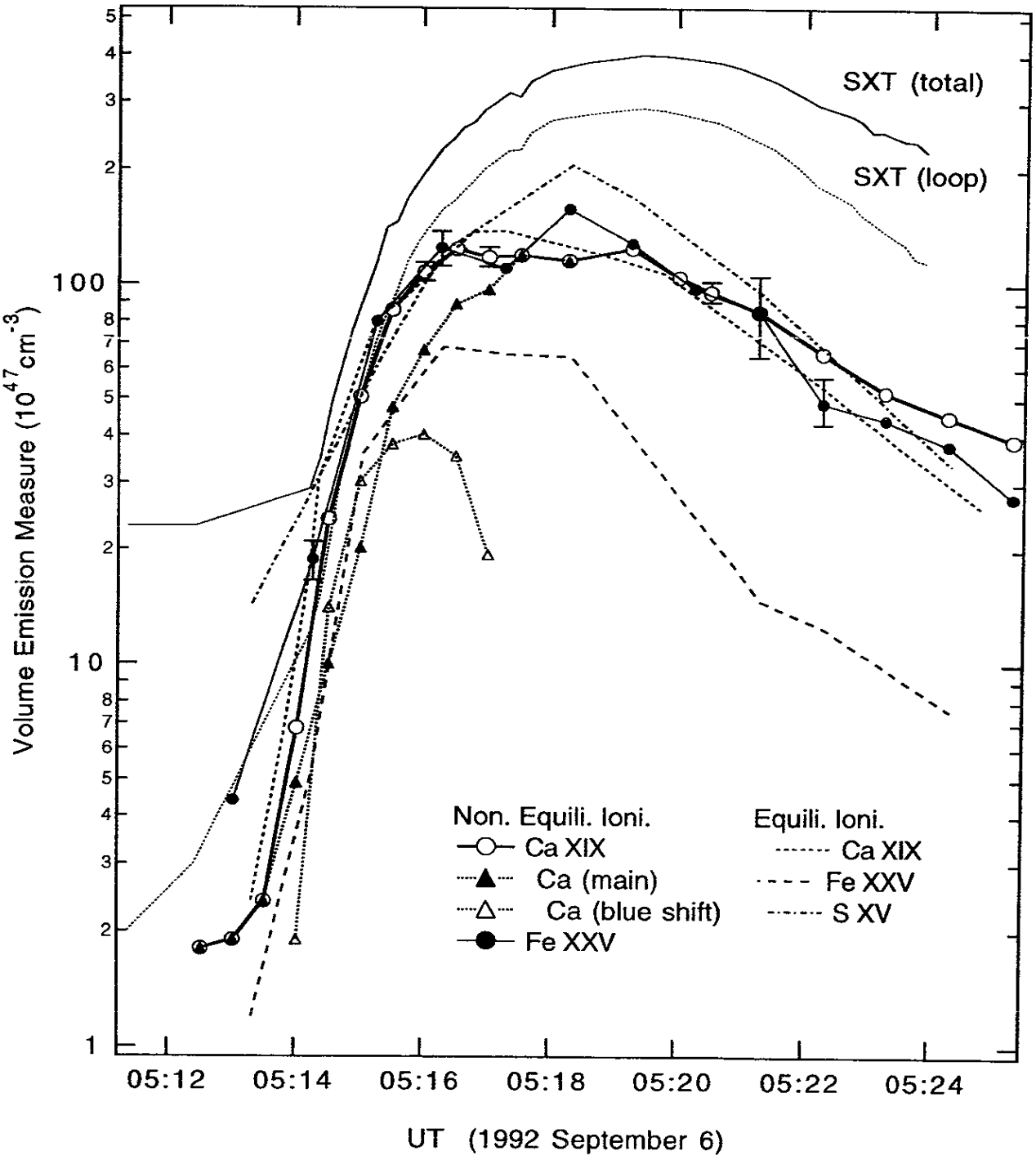
SXT (total)
SXT (loop)
Volume Emission Measure (10^{47}cm^{-3})
100
10
1
Non. Equili. Ioni.
Ca XIX
Ca (main)
Ca (blue shift)
Fe XXV
Equili. Ioni.
Ca XIX
Fe XXV
S XV
05:12
05:14
05:16
05:18
05:20
05:22
05:24
UT (1992 September 6)

Fig.10

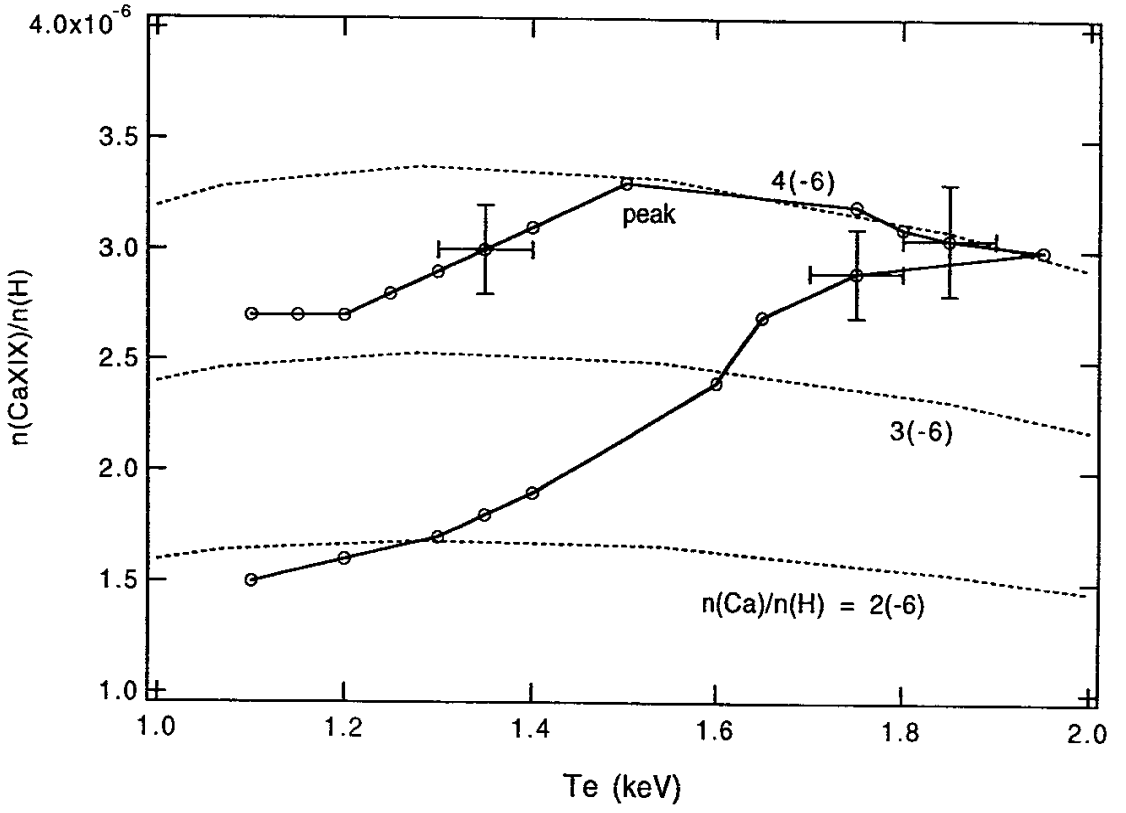

Fig.11(a)

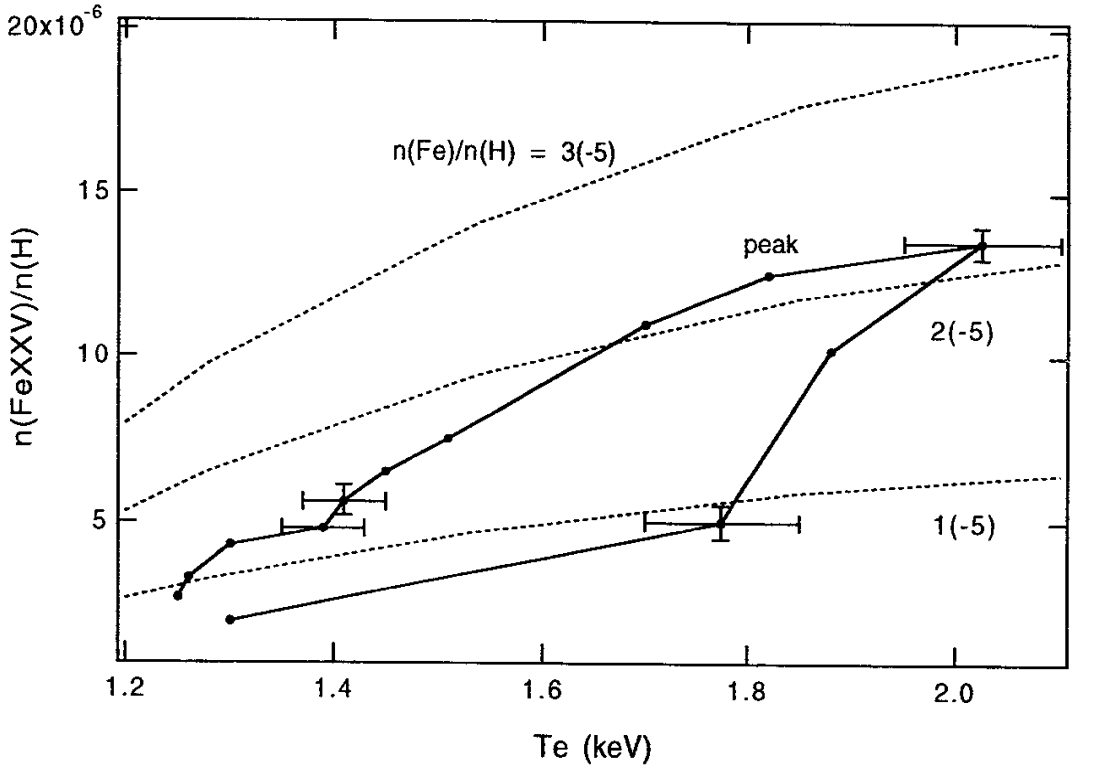

Fig.11(b)

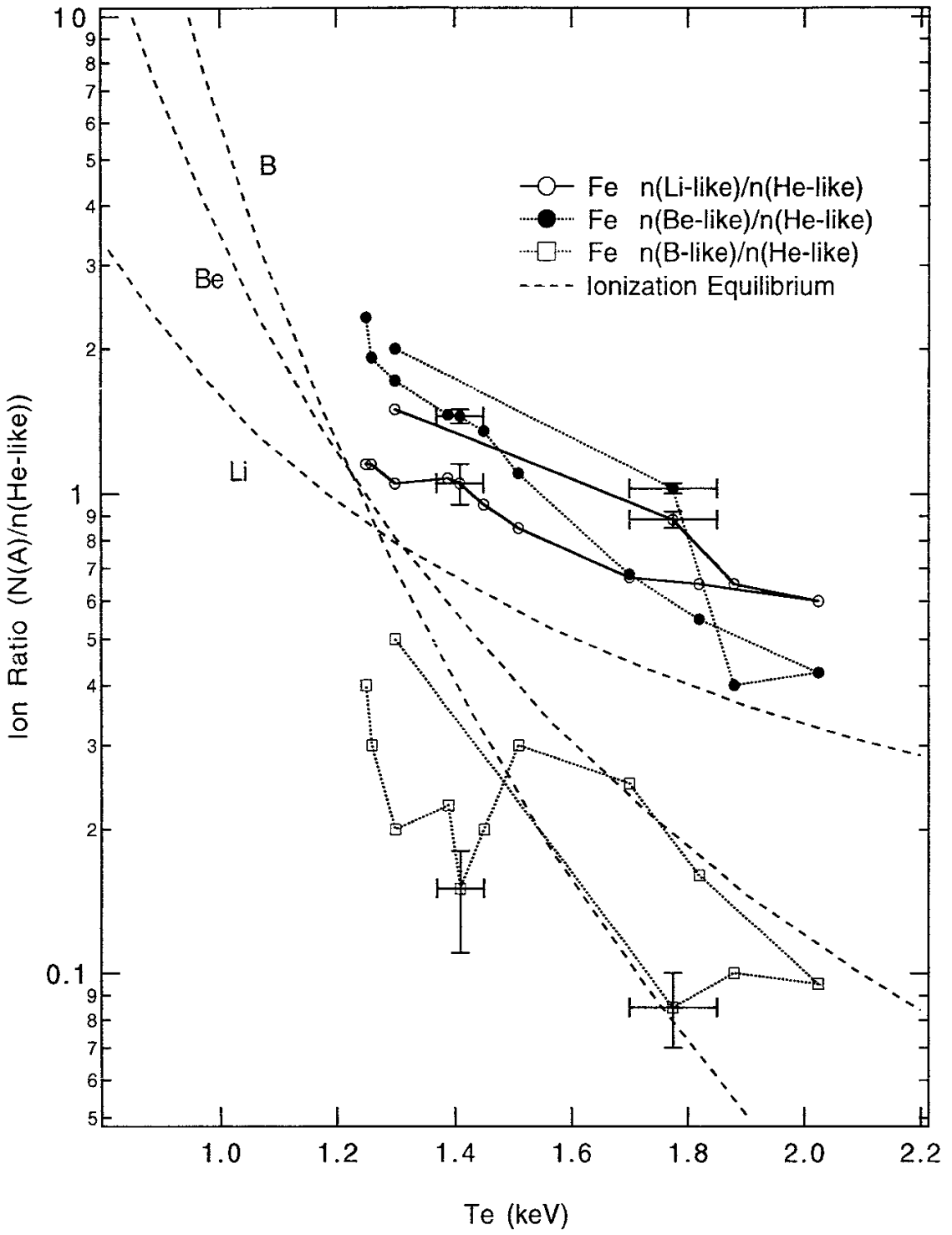
Fe n(Li-like)/n(He-like)
Fe n(Be-like)/n(He-like)
Fe n(B-like)/n(He-like)
Ionization Equilibrium
B
Be
Li
Ion Ratio (N(A)/n(He-like))
Te (keV)
10
1
0.1
1.0
1.2
1.4
1.6
1.8
2.0
2.2

Fig.12 (a)

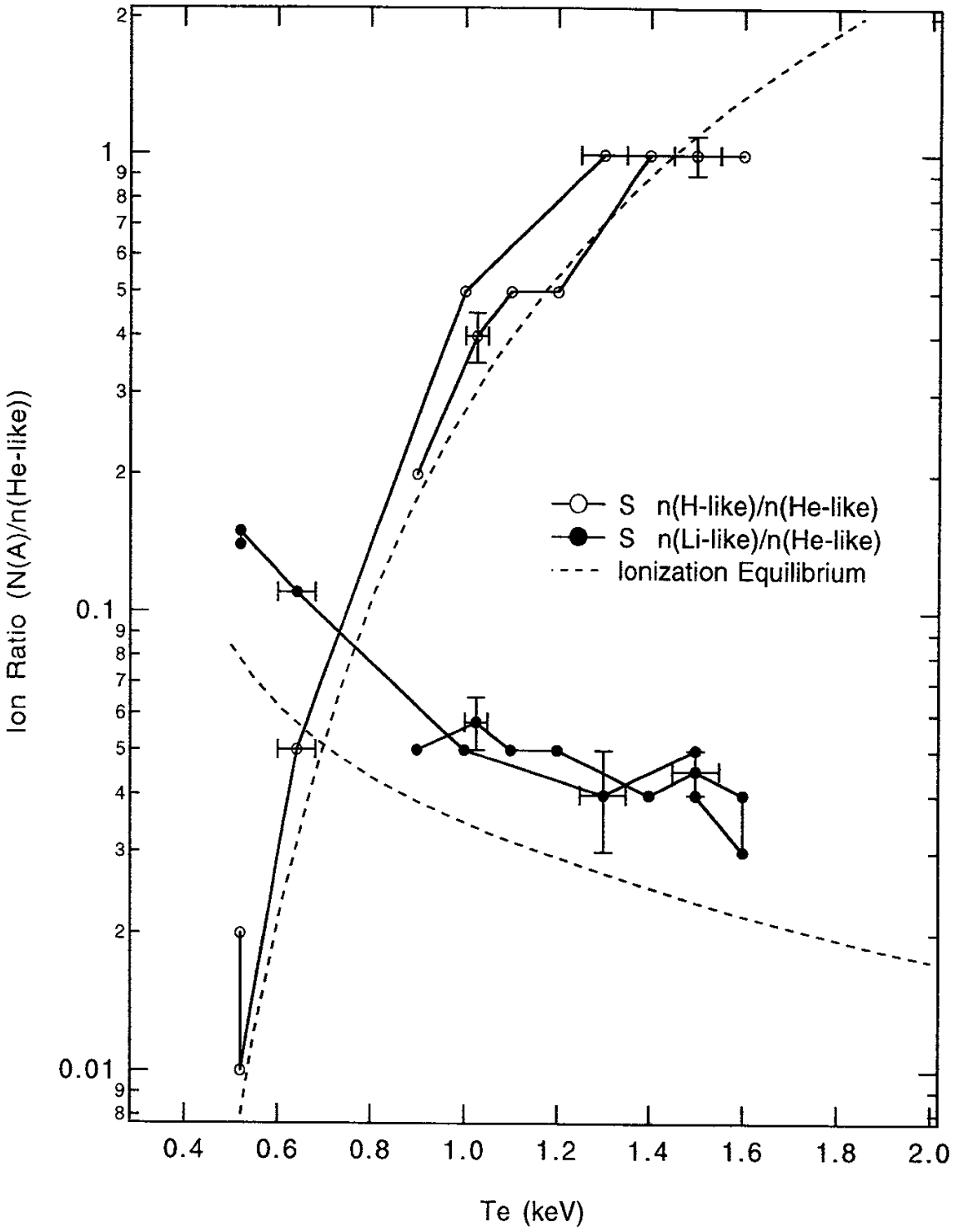
Ion Ratio (N(A)/n(He-like))
Te (keV)
S n(H-like)/n(He-like)
S n(Li-like)/n(He-like)
Ionization Equilibrium
2
1
0.1
0.01
0.4
0.6
0.8
1.0
1.2
1.4
1.6
1.8
2.0

Fig.12 (b)

Fig. 13

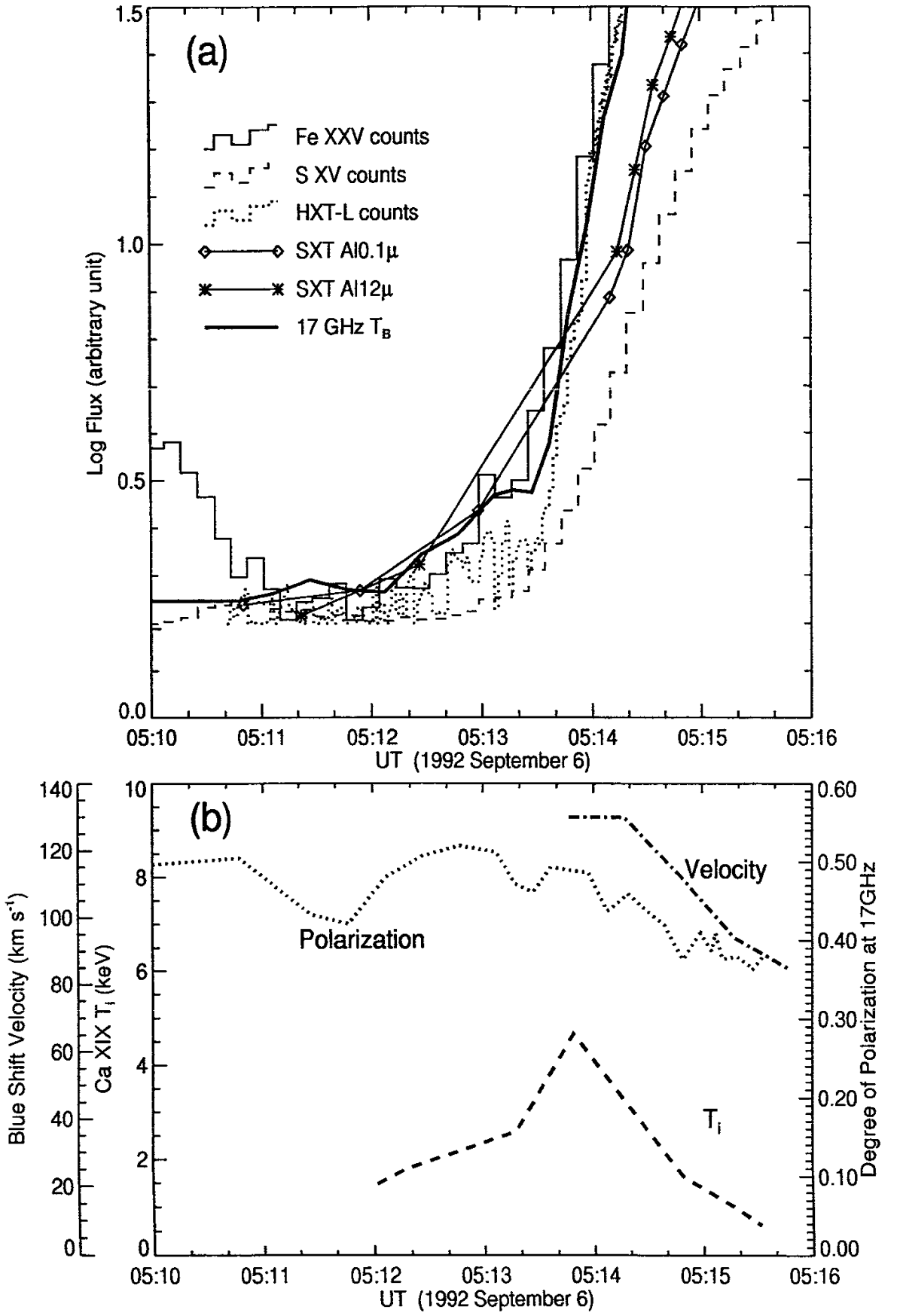
(a)
Fe XXV counts
S XV counts
HXT-L counts
SXT Al0.1μ
SXT Al12μ
17 GHz T_B
Log Flux (arbitrary unit)
1.5
1.0
0.5
0.0
05:10
05:11
05:12
05:13
05:14
05:15
05:16
UT (1992 September 6)
(b)
Velocity
Polarization
T_i
Blue Shift Velocity (km s^{-1})
Ca XIX T_i (keV)
Degree of Polarization at 17GHz
140
120
100
80
60
40
20
0
10
8
6
4
2
0
0.60
0.50
0.40
0.30
0.20
0.10
0.00
05:10
05:11
05:12
05:13
05:14
05:15
05:16
UT (1992 September 6)

Recent Issues of NIFS Series

NIFS-349 J. Xu, K. Ida and J. Fujita,
A Note for Pitch Angle Measurement of Magnetic Field in a Toroidal Plasma Using Motional Stark Effect; Apr. 1995

NIFS-350 J. Uramoto,
Characteristics for Metal Plate Penetration of a Low Energy Negative Muonlike or Pionlike Particle Beam: Apr. 1995

NIFS-351 J. Uramoto,
An Estimation of Life Time for A Low Energy Negative Pionlike Particle Beam: Apr. 1995

NIFS-352 A. Taniike,
Energy Loss Mechanism of a Gold Ion Beam on a Tandem Acceleration System: May 1995

NIFS-353 A. Nishizawa, Y. Hamada, Y. Kawasumi and H. Iguchi,
Increase of Lifetime of Thallium Zeolite Ion Source for Single-Ended Accelerator: May 1995

NIFS-354 S. Murakami, N. Nakajima, S. Okamura and M. Okamoto,
Orbital Aspects of Reachable β Value in NBI Heated Heliotron/Torsatrons; May 1995

NIFS-355 H. Sugama and W. Horton,
Neoclassical and Anomalous Transport in Axisymmetric Toroidal Plasmas with Electrostatic Turbulence; May 1995

NIFS-356 N. Ohyabu
A New Boundary Control Scheme for Simultaneous Achievement of H-mode and Radiative Cooling (SHC Boundary); May 1995

NIFS-357 Y. Hamada, K.N. Sato, H. Sakakita, A. Nishizawa, Y. Kawasumi, R. Liang, K. Kawahata, A. Ejiri, K. Toi, K. Narihara, K. Sato, T. Seki, H. Iguchi, A. Fujisawa, K. Adachi, S. Hidekuma, S. Hirokura, K. Ida, M. Kojima, J. Koong, R. Kumazawa, H. Kuramoto, T. Minami,. M. Sasao, T. Tsuzuki, J.Xu, I. Yamada, and T. Watari,
Large Potential Change Induced by Pellet Injection in JIPP T-IIU Tokamak Plasmas; May 1995

NIFS-358 M. Ida and T. Yabe,
Implicit CIP (Cubic-Interpolated Propagation) Method in One Dimension; May 1995

NIFS-359 A. Kageyama, T. Sato and The Complexity Simulation Group,
Computer Has Solved A Historical Puzzle: Generation of Earth's Dipole

Field; June 1995

NIFS-360 K. Itoh, S.-I. Itoh, M. Yagi and A. Fukuyama,
Dynamic Structure in Self-Sustained Turbulence; June 1995

NIFS-361 K. Kamada, H. Kinoshita and H. Takahashi,
Anomalous Heat Evolution of Deuteron Implanted Al on Electron Bombardment; June 1995

NIFS-362 V.D. Pustovitov,
Suppression of Pfirsch-schlüter Current by Vertical Magnetic Field in Stellarators; June 1995

NIFS-363 A. Ida, H. Sanuki and J. Todoroki
An Extended K-dV Equation for Nonlinear Magnetosonic Wave in a Multi-Ion Plasma; June 1995

NIFS-364 H. Sugama and W. Horton
Entropy Production and Onsager Symmetry in Neoclassical Transport Processes of Toroidal Plasmas; July 1995

NIFS-365 K. Itoh, S.-I. Itoh, A. Fukuyama and M. Yagi,
On the Minimum Circulating Power of Steady State Tokamaks; July 1995

NIFS-366 K. Itoh and Sanae-I. Itoh,
The Role of Electric Field in Confinement; July 1995

NIFS-367 F. Xiao and T. Yabe,
A Rational Function Based Scheme for Solving Advection Equation; July 1995

NIFS-368 Y. Takeiri, O. Kaneko, Y. Oka, K. Tsumori, E. Asano, R. Akiyama, T. Kawamoto and T. Kuroda,
Multi-Beamlet Focusing of Intense Negative Ion Beams by Aperture Displacement Technique; Aug. 1995

NIFS-369 A. Ando, Y. Takeiri, O. Kaneko, Y. Oka, K. Tsumori, E. Asano, T. Kawamoto, R. Akiyama and T. Kuroda,
Experiments of an Intense H- Ion Beam Acceleration; Aug. 1995

NIFS-370 M. Sasao, A. Taniike, I. Nomura, M. Wada, H. Yamaoka and M. Sato,
Development of Diagnostic Beams for Alpha Particle Measurement on ITER; Aug. 1995

NIFS-371 S. Yamaguchi, J. Yamamoto and O. Motojima;
A New Cable -in conduit Conductor Magnet with Insulated Strands; Sep. 1995

NIFS-372 H. Miura,

Enstrophy Generation in a Shock-Dominated Turbulence; Sep. 1995

NIFS-373 M. Natsir, A. Sagara, K. Tsuzuki, B. Tsuchiya, Y. Hasegawa, O. Motojima, *Control of Discharge Conditions to Reduce Hydrogen Content in Low Z Films Produced with DC Glow;* Sep. 1995

NIFS-374 K. Tsuzuki, M. Natsir, N. Inoue, A. Sagara, N. Noda, O. Motojima, T. Mochizuki, I. Fujita, T. Hino and T. Yamashina, *Behavior of Hydrogen Atoms in Boron Films during H_2 and He Glow Discharge and Thermal Desorption;* Sep. 1995

NIFS-375 U. Stroth, M. Murakami, R.A. Dory, H. Yamada, S. Okamura, F. Sano and T. Obiki, *Energy Confinement Scaling from the International Stellarator Database*; Sep. 1995

NIFS-376 S. Bazdenkov, T. Sato, K. Watanabe and The Complexity Simulation Group, *Multi-Scale Semi-Ideal Magnetohydrodynamics of a Tokamak Plasma;* Sep. 1995

NIFS-377 J. Uramoto, *Extraction of Negative Pionlike Particles from a H2 or D2 Gas Discharge Plasma in Magnetic Field;* Sep. 1995

NIFS-378 K. Akaishi, *Theoretical Consideration for the Outgassing Characteristics of an Unbaked Vacuum System*; Oct. 1995

NIFS-379 H. Shimazu, S. Machida and M. Tanaka, *Macro-Particle Simulation of Collisionless Parallel Shocks*; Oct. 1995

NIFS-380 N. Kondo and Y. Kondoh, *Eigenfunction Spectrum Analysis for Self-organization in Dissipative Solitons;* Oct. 1995

NIFS-381 Y. Kondoh, M. Yoshizawa, A. Nakano and T. Yabe, *Self-organization of Two-dimensional Incompressible Viscous Flow in a Friction-free Box;* Oct. 1995

NIFS-382 Y.N. Nejoh and H. Sanuki, *The Effects of the Beam and Ion Temperatures on Ion-Acoustic Waves in an Electron Beam-Plasma System;* Oct. 1995

NIFS-383 K. Ichiguchi, O. Motojima, K. Yamazaki, N. Nakajima and M. Okamoto *Flexibility of LHD Configuration with Multi-Layer Helical Coils;* Nov. 1995

NIFS-384 D. Biskamp, E. Schwarz and J.F. Drake, *Two-dimensional Electron Magnetohydrodynamic Turbulence*; Nov. 1995

NIFS-385 H. Kitabata, T. Hayashi, T. Sato and Complexity Simulation Group,
Impulsive Nature in Collisional Driven Reconnection; Nov. 1995

NIFS-386 Y. Katoh, T. Muroga, A. Kohyama, R.E. Stoller, C. Namba and O. Motojima,
Rate Theory Modeling of Defect Evolution under Cascade Damage Conditions:The Influence of Vacancy-type Cascade Remnants and Application to the Defect Production Chracterization by Microstructural Analysis; Nov. 1995

NIFS-387 K. Araki, S. Yanase and J. Mizushima,
Symmetry Breaking by Differential Rotation and Saddle-node Bifurcation of the Thermal Convection in a Spherical Shell; Dec. 1995

NIFS-388 V.D. Pustovitov,
Control of Pfirsch-Schlüter Current by External Poloidal Magnetic Field in Conventional Stellarators: Dec. 1995

NIFS-389 K. Akaishi,
On the Outgassing Rate Versus Time Characteristics in the Pump-down of an Unbaked Vacuum System; Dec. 1995

NIFS-390 K.N. Sato, S. Murakami, N. Nakajima, K. Itoh,
Possibility of Simulation Experiments for Fast Particle Physics in Large Helical Device (LHD); Dec. 1995

NIFS-391 W.X.Wang, M. Okamoto, N. Nakajima, S. Murakami and N. Ohyabu,
A Monte Carlo Simulation Model for the Steady-State Plasma in the Scrape-off Layer; Dec. 1995

NIFS-392 Shao-ping Zhu, R. Horiuchi, T. Sato and The Complexity Simulation Group,
Self-organization Process of a Magnetohydrodynamic Plasma in the Presence of Thermal Conduction; Dec. 1995

NIFS-393 M. Ozaki, T. Sato, R. Horiuchi and the Complexity Simulation Group
Electromagnetic Instability and Anomalous Resistivity in a Magnetic Neutral Sheet; Dec. 1995

NIFS-394 K. Itoh, S.-I Itoh, M. Yagi and A. Fukuyama,
Subcritical Excitation of Plasma Turbulence; Jan. 1996

NIFS-395 H. Sugama and M. Okamoto, W. Horton and M. Wakatani,
Transport Processes and Entropy Production in Toroidal Plasmas with Gyrokinetic Eletromagnetic Turbulence; Jan. 1996

NIFS-396 T. Kato, T. Fujiwara and Y. Hanaoka,
X-ray Spectral Analysis of Yohkoh BCS Data on Sep. 6 1992 Flares - Blue Shift Component and Ion Abundances -; Feb. 1996